Multiobjective Optimization of a Four-Step Adsorption Process for Postcombustion CO_2 Capture Via Finite Volume Simulation

Reza Haghpanah,[†] Aniruddha Majumder,[†] Ricky Nilam,[†] Arvind Rajendran,*,[†] Shamsuzzaman Farooq,*,[‡] Iftekhar A. Karimi,[‡] and Mohammad Amanullah[†]

[†]School of Chemical and Biomedical Engineering, Nanyang Technological University, 62 Nanyang Drive, Singapore 637459
[‡]Department of Chemical and Biomolecular Engineering, National University of Singapore, 4 Engineering Drive 4, Singapore 117576

Ⓢ Supporting Information

ABSTRACT: In this study, we first report the development of a robust and efficient finite volume based adsorption process simulator, essential for rigorous optimization of a transient cyclic operation without resorting to any model reduction. We present a detailed algorithm for the common boundary conditions encountered in nonisothermal and nonisobaric adsorption process simulations. A comprehensive comparison of the high-resolution total variation diminishing (TVD) schemes, namely, van Leer and Superbee, with the weighted essentially nonoscillatory (WENO) finite volume scheme is performed, and trade-off plots are presented to identify the numerical scheme most suitable for attaining speed and accuracy at the same time. The simulator is then used to perform rigorous optimization of a four-step process for postcombustion CO_2 capture from dry flue gas on zeolite 13X. The aim is to identify operating conditions at which the purity and recovery demands are met and to calculate corresponding energy consumption and process productivity. The purity−recovery and energy−productivity Paretos are generated using multiobjective optimization. It is shown that, for a strict vacuum swing adsorption (VSA) process, an evacuation pressure of 0.02 bar is required to satisfy regulatory demands of attaining a CO_2 purity and recovery of 90%. It is also quantitatively shown that pressurizing the flue gas is detrimental to the energy consumption of process, although offering improvement in productivity.

1. INTRODUCTION

It is now widely accepted by the scientific community that anthropogenic greenhouse gases, chiefly CO_2, are the sources of global warming. There are several technical approaches to mitigate and control CO_2 emissions from the combustion of fossil fuels. The ideal solution will be to substitute nonrenewable hydrocarbon-based energy sources with renewable ones. However, the current techno-economic status of renewable energy options, the large number of fossil fuel based power plants in operation, and the availability of cheap and abundant coal make large scale deployment of renewable energy options prohibitively expensive in the near future.[1] Hence, it is important to develop technologies that will allow continued operation of fossil fuel based power plants, while reducing CO_2 emissions. Carbon capture and storage, which seeks to separate CO_2 from flue gas and sequester it permanently, is advocated as an important near-to-midterm measure to contain the rising atmospheric CO_2 concentration. Recent studies indicate that the cyclic adsorption processes are promising options for CO_2 capture.[2−4]

Adsorption separation processes alternate between adsorption and desorption modes of operation. Depending on the type of operation, pressure swing adsorption (PSA) or temperature swing adsorption (TSA), the intensive variable that is altered is pressure or temperature. In PSA, the adsorption step is performed at a higher pressure compared to the desorption step, while in TSA the adsorption step is carried out at a lower temperature than the desorption step. The early PSA cycles were operated between an above-atmospheric pressure for adsorption and atmospheric pressure for desorption. Lowering the desorption pressure to vacuum level offers a higher working capacity, especially when the isotherm is highly nonlinear. This is called vacuum swing adsorption (VSA) to distinguish it from PSA. Cycles with adsorption at above-atmospheric pressure and desorption by evacuation, called pressure−vacuum swing adsorption (PVSA), have also been proposed.[5] Some industrial applications of the PSA processes are air separation for nitrogen purification,[6−8] air drying,[9,10] hydrogen purification,[11,12] and hydrocarbon separation.[13,14] The present generation of adsorptive air separation for oxygen production is an example of industrial application of VSA.[15] Most industrial PSA processes have been designed and optimized for high purity and recovery of the weaker (lighter) adsorbate in the raffinate product. However, the recovery of the high-purity stronger (heavier) component in the extract product is also possible, and it is receiving increasing attention, e.g., CO_2 capture and concentration (CCC) from flue gas for greenhouse gas mitigation.[16−20] Both VSA and PVSA cycles have been investigated for CCC. A PVSA process is an obvious choice when the feed mixture is available at above-atmospheric pressure, but it is not high enough to achieve the desired separation with atmospheric desorption. However, the consequences of pressurizing postcombustion flue gas, which is released at atmospheric pressure, on the energy consumption and productivity of the process have not been adequately addressed in the literature.[19,21]

Table 1. Finite Volume Studies in the Literature for Adsorption Processes[a]

reference	process	type of simulation	thermal condition	pressure drop	isotherm	numerical scheme
26	adsorption	DCB	isothermal	yes	linear	adaptive QUICK
27	adsorption	PSA	nonisothermal	yes	nonlinear	adaptive QUICK
28	adsorption	PSA	isothermal	yes	nonlinear	QUICK and SMART
30	chromatography	pulse injection	isothermal	no	nonlinear	HR
31	chromatography	pulse injection	isothermal	no	nonlinear	HR
34	chromatography	pulse injection	isothermal	no	linear	adaptive multiresolution
current study	adsorption	DCB/PSA	nonisothermal	yes	nonlinear	HR and WENO

[a]HR, high resolution; DCB, dynamic column breakthrough.

In order to rigorously optimize cyclic adsorption processes using detailed models, robust numerical simulation techniques are essential. The chosen scheme should be fast and robust enough to handle stiff problems, while capturing the process dynamics and performance accurately. Owing to the nature of the conservation equations, sharp fronts of concentration and temperature may propagate along the adsorption column. Ensuring the accuracy and stability of the simulation program in such situations is a challenge, especially when dealing with highly nonlinear isotherms, e.g., CO_2 adsorption on zeolite 13X.

Several schemes for simulating adsorption processes, such as finite difference,[22] orthogonal collocation,[23] finite element,[24] combinations thereof,[25] and finite volume,[26−28] have been used. Recent literature suggests that the finite volume method offers the stability and robustness for a wide range of systems.[29−31] It solves the integral rather than the differential forms of the conservation equations, thus allowing better closure of mass, energy, and momentum balances. In cases where sharp discontinuities propagate in the system, high-resolution total variation diminishing (TVD)[29] and weighted essentially nonoscillatory (WENO)[32] methods whave been successfully implemented within the framework of the finite volume method to reduce the nonphysical oscillations around discontinuities, while still capturing the smooth portion of the solution. The TVD schemes achieve these by employing flux limiters, while ensuring higher-order (>1) accuracy. In summary, high-resolution TVD schemes combine the accuracy of higher-order methods with the stability of lower-order methods. In the WENO scheme, a convex combination of lower-order fluxes is used to obtain a higher-order approximation.[32] In this scheme, a nonlinear adaptive procedure is used to automatically choose the locally smoothest stencil to avoid nonphysical oscillations near discontinuities.[33] [A stencil is the weighted sum of neighboring cell(s).]

Finite volume methods have been used to simulate a variety of adsorption processes as summarized in Table 1. Webley and He[26] demonstrated an isothermal, nonisobaric breakthrough simulation with a linear isotherm using the adaptive quadratic upstream interpolation (QUICK) method. In the proposed scheme, an exponential smoothing function was used, since the unbounded QUICK scheme gives oscillatory results in the presence of sharp gradients. The adaptive QUICK method was later extended to a more general case of nonisothermal and nonisobaric PSA simulation to describe experimental data.[27] However, one shortcoming of this approach is that the smoothing parameters are problem-dependent and hence require tuning. Cruz et al.[28] demonstrated the advantages of a high-resolution finite volume scheme using the flux limiter SMART (sharp and monotonic algorithm for realistic transport) over an unbounded QUICK method for PSA simulation under isothermal condition. More recently, a comparison of high-resolution schemes has been reported for the simulation of chromatographic systems.[30,31,34] All these studies have proven the capabilities of a semi-discrete, adaptive finite volume technique in handling sharp fronts.

From the above discussion, high-resolution finite volume schemes with flux limiters and WENO appear to have favorable performance characteristics in terms of accuracy, stability, and speed. However, no study, to our knowledge, has presented a detailed comparative evaluation of these methods for the most general case of PVSA simulations accounting for heat effect, pressure drop, velocity variations due to adsorption/desorption, and isotherm nonlinearity. In this context, the main contributions of this study are the following:

- to present the details of an efficient finite volume scheme for the most general case of PVSA simulations accounting for heat effect, pressure drop, velocity variations due to adsorption/desorption, and isotherm nonlinearity
- to provide a comprehensive comparison of two high-resolution TVD schemes, van Leer and Superbee, and WENO together with the finite difference method in terms of trade-off plots for convergence characteristics and computational efficiencies
- to perform multiobjective optimization of a simple four-step PVSA cycle to identify the operating conditions that minimize energy penalty and maximize productivity, while meeting the stringent purity−recovery constraints for CCC on zeolite 13X from postcombustion power plant flue gas
- to study the effect of flue gas pressurization on the four-step process performance

2. MODEL EQUATIONS

In this work, we consider a column of length L packed with a solid adsorbent as shown in Figure 1. The following assumptions are used to derive the constitutive transport equations.

- An axially dispersed plug flow model is used to represent the bulk fluid flow.
- The gas phase is described by the ideal gas law.
- The solid phase mass transfer rate is described by the linear driving force (LDF) model.
- Darcy's law is used to account for the frictional pressure drop in the axial direction.
- Thermal equilibrium between the gas and solid phases is established instantaneously.
- No concentration, temperature, and pressure gradients exist in the radial direction.
- Heat transfer occurs across the column wall whose outer surface is maintained at a constant temperature.
- The adsorbent properties and bed voidage are uniform across the column.

The above assumptions result in ($n_{comp} - 1$) component mass balances, total mass balance, and energy balances through the column and across the column wall. The detailed equations
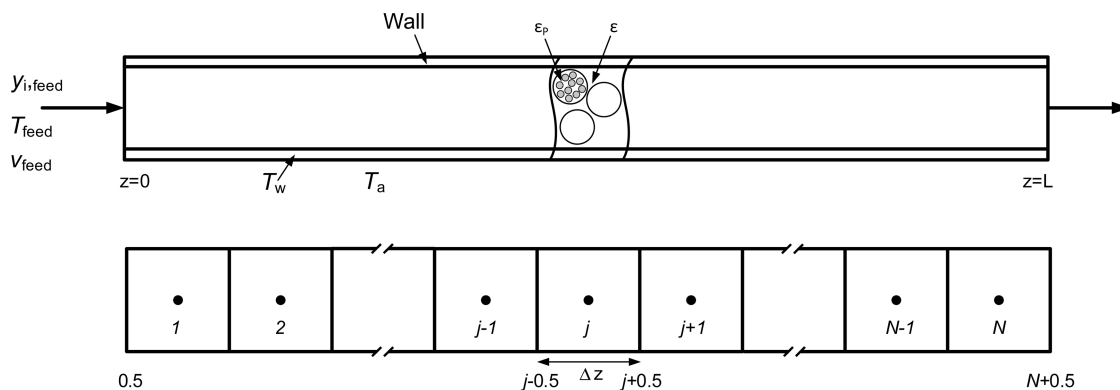
Figure 1. Schematic of the adsorption column and finite volume discretization scheme.

in dimensional form are provided in the Appendix, while the definitions of all variables are provided in the Nomenclature. The essential equations and boundary conditions in dimensionless form are as follows, with coefficients and parameters listed in Table 1 available in the Supporting Information.

component mass balance:

$$\frac{\partial y_i}{\partial \tau} = \frac{1}{Pe}\frac{\bar{T}}{\bar{P}}\frac{\partial}{\partial Z}\left(\frac{\bar{P}}{\bar{T}}\frac{\partial y_i}{\partial Z}\right) - \frac{\bar{T}}{\bar{P}}\frac{\partial}{\partial Z}\left(\frac{y_i\bar{P}}{\bar{T}}\bar{v}\right) - \psi\frac{\bar{T}}{\bar{P}}\frac{\partial x_i}{\partial \tau}$$
$$- \frac{y_i}{\bar{P}}\frac{\partial \bar{P}}{\partial \tau} + \frac{y_i}{\bar{T}}\frac{\partial \bar{T}}{\partial \tau} \tag{1}$$

total mass balance:

$$\frac{\partial \bar{P}}{\partial \tau} = -\bar{T}\frac{\partial}{\partial Z}\left(\frac{\bar{P}}{\bar{T}}\bar{v}\right) - \psi\bar{T}\sum_{i=1}^{n_{comp}}\frac{\partial x_i}{\partial \tau} + \frac{\bar{P}}{\bar{T}}\frac{\partial \bar{T}}{\partial \tau} \tag{2}$$

solid phase balance:

$$\frac{\partial x_i}{\partial \tau} = \alpha_i(x_i^* - x_i) \tag{3}$$

column energy balance:

$$\frac{\partial \bar{T}}{\partial \tau} = \Omega_1\frac{\partial^2 \bar{T}}{\partial Z^2} - \Omega_2\frac{\partial}{\partial Z}(\bar{v}\bar{P}) - \Omega_3\bar{T}\sum_{i=1}^{n_{comp}}\frac{\partial x_i}{\partial \tau}$$
$$+ \sum_{i=1}^{n_{comp}}\left(\sigma_i\frac{\partial x_i}{\partial \tau}\right) - \Omega_4(\bar{T} - \bar{T}_w) - \Omega_2\frac{\partial \bar{P}}{\partial \tau} \tag{4}$$

wall energy balance:

$$\frac{\partial \bar{T}_w}{\partial \tau} = \Pi_1\frac{\partial^2 \bar{T}_w}{\partial Z^2} + \Pi_2(\bar{T} - \bar{T}_w) - \Pi_3(\bar{T}_w - \bar{T}_a) \tag{5}$$

pressure drop:

$$-\frac{\partial \bar{P}}{\partial Z} = \frac{150}{4}\frac{1}{r_p^2}\left(\frac{1-\varepsilon}{\varepsilon}\right)^2\frac{v_0 L}{P_0}\mu\bar{v} \tag{6}$$

Rearranging eq 6 provides an expression to compute the local velocity:

$$\bar{v} = \frac{4}{150}\left(\frac{\varepsilon}{1-\varepsilon}\right)^2 r_p^2 \frac{P_0}{\mu v_0 L}\left(-\frac{\partial \bar{P}}{\partial Z}\right) \tag{7}$$

The solution of the above equations requires appropriate initial and boundary conditions. Typical initial conditions assume the column to be saturated with a known composition

of gas at a particular temperature and pressure. The dimensionless boundary conditions, generalized as open−open, open−closed and closed−open, as shown in Figure 2 and detailed in the Appendix, are given below:
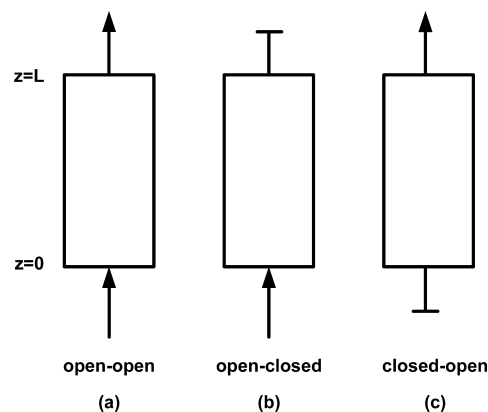

Figure 2. Typical steps in a cyclic adsorption process: (a) open−open; (b) open−closed; (c) closed−open.

Open−Open: For the component mass balance, the Danckwert's boundary conditions for a dispersed plug flow system apply:

$$\left.\frac{\partial y_i}{\partial Z}\right|_{Z=0} = -\bar{v}_{Z=0}Pe(y_{i,\text{feed}} - y_i|_{Z=0}) \tag{8}$$

$$\left.\frac{\partial y_i}{\partial Z}\right|_{Z=1} = 0 \tag{9}$$

The boundary conditions for eq 4 are obtained by invoking the analogy between mass and heat transfer:

$$\left.\frac{\partial \bar{T}}{\partial Z}\right|_{Z=0} = -\bar{v}_{Z=0}Pe_h(\bar{T}_{\text{feed}} - \bar{T}|_{Z=0}) \tag{10}$$

$$\left.\frac{\partial \bar{T}}{\partial Z}\right|_{Z=1} = 0 \tag{11}$$

The boundary conditions for eq 5 are given by

$$\bar{T}_w|_{Z=0} = \bar{T}_w|_{Z=1} = \bar{T}_a \tag{12}$$

Due to eq 7, the total mass balance equation (eq 2) is in effect second order in pressure; hence two boundary conditions are required. The exit pressure is used as one boundary condition, i.e.

$$\bar{P}|_{Z=1} = 1 \tag{13}$$

while the inlet pressure is calculated from eq 6 using a known inlet velocity, i.e.

$$\bar{v}|_{Z=0} = 1 \tag{14}$$

Open−Closed: The boundary conditions for eqs 1, 2, 4, and 5 are identical to those for the open−open case, i.e., eq 8−12. The velocity, $\bar{v}|_{Z=0}$, is calculated from the change in pressure at the column inlet. Since the end at $Z = 1$ is closed, $\bar{v}|_{Z=1} = 0$, and by using eq 7 the boundary condition for pressure at this end is

$$\left.\frac{\partial \bar{P}}{\partial Z}\right|_{Z=1} = 0 \tag{15}$$

Closed−Open: In the closed−open case, $\bar{v}|_{Z=0} = 0$. Equations 9, 11, and 12 are not affected, while eqs 8 and 10 reduce to eqs 16 and 17, respectively:

$$\left.\frac{\partial y_i}{\partial Z}\right|_{Z=0} = 0 \tag{16}$$

$$\left.\frac{\partial \bar{T}}{\partial Z}\right|_{Z=0} = 0 \tag{17}$$

The boundary condition for pressure at $Z = 0$ is

$$\left.\frac{\partial \bar{P}}{\partial Z}\right|_{Z=0} = 0 \tag{18}$$

$\bar{v}|_{Z=1}$ is calculated from the change in pressure at the column outlet.

3. FINITE VOLUME METHOD FOR ADSORPTION SIMULATION

In this section, we discuss the spatial discretization for the finite volume method and its implementation. In this approach, the column is divided into N cells, each with a volume of ΔV, as shown in Figure 1. Any conserved quantity, f, is approximated by a cell average given by

$$f_j(t) = \frac{1}{\Delta V}\int_{V_j} f(t)\, dV \tag{19}$$

where j represents the cell index.

The spatial derivatives in the transport equations are converted to algebraic expressions by integrating over each cell j with boundaries denoted as $j − 0.5$ and $j + 0.5$. Note that f_j denotes the value at the center of cell j. Then, eqs 1−5 in the discretized form are listed below.

component mass balance (eq 1):

$$\frac{\partial y_{i,j}}{\partial \tau} = \frac{1}{Pe}\frac{\bar{T}_j}{\bar{P}_j}\frac{1}{\Delta Z}\left(\left.\frac{\bar{P}}{\bar{T}}\right|_{j+0.5}\frac{y_{i,j+1} - y_{i,j}}{\Delta Z} - \left.\frac{\bar{P}}{\bar{T}}\right|_{j-0.5}\right.$$
$$\left.\times \frac{y_{i,j} - y_{i,j-1}}{\Delta Z}\right) - \frac{\bar{T}_j}{\bar{P}_j}\frac{1}{\Delta Z}\left(\left.\frac{y_i\bar{P}}{\bar{T}}\bar{v}\right|_{j+0.5} - \left.\frac{y_i\bar{P}}{\bar{T}}\bar{v}\right|_{j-0.5}\right)$$
$$- \psi\frac{\bar{T}_j}{\bar{P}_j}\frac{\partial x_{i,j}}{\partial \tau} - \frac{y_{i,j}}{\bar{P}_j}\frac{\partial \bar{P}_j}{\partial \tau} + \frac{y_{i,j}}{\bar{T}_j}\frac{\partial \bar{T}_j}{\partial \tau} \tag{20}$$

total mass balance (eq 2):

$$\frac{\partial \bar{P}_j}{\partial \tau} = -\frac{\bar{T}_j}{\Delta Z}\left(\left.\frac{\bar{P}}{\bar{T}}\bar{v}\right|_{j+0.5} - \left.\frac{\bar{P}}{\bar{T}}\bar{v}\right|_{j-0.5}\right) - \psi\bar{T}_j\sum_{i=1}^{n_{comp}}\frac{\partial x_{i,j}}{\partial \tau}$$
$$+ \frac{\bar{P}_j}{\bar{T}_j}\frac{\partial \bar{T}_j}{\partial \tau} \tag{21}$$

solid phase balance (eq 3):

$$\frac{\partial x_{i,j}}{\partial \tau} = \alpha_i(x_{i,j}^* - x_{i,j}) \tag{22}$$

column energy balance (eq 4):

$$\frac{\partial \bar{T}_j}{\partial \tau} = \Omega_{1,j}\frac{1}{\Delta Z}\left(\frac{\bar{T}_{j+1} - \bar{T}_j}{\Delta Z} - \frac{\bar{T}_j - \bar{T}_{j-1}}{\Delta Z}\right)$$
$$- \Omega_{2,j}\frac{1}{\Delta Z}(\bar{v}\bar{P}|_{j+0.5} - \bar{v}\bar{P}|_{j-0.5}) - \Omega_{3,j}\bar{T}_j\sum_{i=1}^{n_{comp}}\frac{\partial x_{i,j}}{\partial \tau}$$
$$+ \sum_{i=1}^{n_{comp}}\left(\sigma_{i,j}\frac{\partial x_{i,j}}{\partial \tau}\right) - \Omega_{4,j}(\bar{T}_j - \bar{T}_{w,j}) - \Omega_{2,j}\frac{\partial \bar{P}_j}{\partial \tau} \tag{23}$$

wall energy balance (eq 5):

$$\frac{\partial \bar{T}_{w,j}}{\partial \tau} = \Pi_1\frac{1}{\Delta Z}\left(\frac{\bar{T}_{w,j+1} - \bar{T}_{w,j}}{\Delta Z} - \frac{\bar{T}_{w,j} - \bar{T}_{w,j-1}}{\Delta Z}\right)$$
$$+ \Pi_2(\bar{T}_j - \bar{T}_{w,j}) - \Pi_3(\bar{T}_{w,j} - \bar{T}_{a,j}) \tag{24}$$

It should be noted that the dispersion term in eq 20 is approximated using a combination of forward difference and finite volume schemes. The various finite volume schemes differ in the way they relate the wall values to the node values. In this work, we consider four such schemes, namely, the upwind difference scheme (UDS), van Leer, Superbee, and WENO.

UDS:

$$f_{j+0.5} = f_j \tag{25}$$

TVD:

$$f_{j+0.5} = f_j + \frac{1}{2}\phi(r_{j+0.5})(f_{j+1} - f_j) \tag{26}$$

where

$$r_{j+0.5} = \frac{f_j - f_{j-1} + \delta}{f_{j+1} - f_j + \delta} \tag{27}$$

$r_{j+0.5}$ is the successive slope ratio, which is a measure of the smoothness of the solution. The constant δ is a very small number, typically 10^{-10}. In eq 26, ϕ is the flux limiter function as defined below for the two TVD schemes:

van Leer:

$$\phi(r_{j+0.5}) = \frac{r_{j+0.5} + |r_{j+0.5}|}{1 + |r_{j+0.5}|} \tag{28}$$

Superbee:

$$\phi(r_{j+0.5}) = \max[0, \min(2r_{j+0.5}, 1), \min(r_{j+0.5}, 2)] \tag{29}$$

For the WENO scheme, the relation is given by

$$f_{j+0.5} = \frac{\alpha_{0,j}}{\alpha_{0,j} + \alpha_{1,j}}\left[\frac{1}{2}(f_j + f_{j+1})\right] + \frac{\alpha_{1,j}}{\alpha_{0,j} + \alpha_{1,j}}\left[\frac{3}{2}f_j - \frac{1}{2}f_{j-1}\right] \qquad (30)$$

where

$$\alpha_{0,j} = \frac{2/3}{(f_{j+1} - f_j + \delta)^4}, \qquad \alpha_{1,j} = \frac{1/3}{(f_j - f_{j-1} + \delta)^4} \qquad (31)$$

Note that using UDS reduces the finite volume scheme to a finite difference approximation. While UDS is nonoscillatory and relatively straightforward to implement, it causes numerical dispersion leading to low accuracy. In contrast, the finite volume schemes are established to be more accurate and robust.[29,31,32,35−37]

As seen in eqs 26 and 30, the calculation of the flux at $j + 0.5$ requires the values of the state variable at $j − 1$, j, and $j + 1$. For $j = 2, ..., N − 1$, the calculation is rather straightforward as these values are available. However, for the flux at the right wall of cell 1, we require the values at $j = 0$, 1, and 2. While the values at $j = 1$ and 2 are known, those at $j = 0$ are not. Typically, this issue is overcome by including a ghost cell to the left of cell 1. However, in this work, we avoid this and instead use the half-cell approximation; i.e., we assume that the change from $f_{0.5}$ to f_1 is the same as that from f_0 to $f_{0.5}$. In eqs 25−31, the following half-cell approximation is applied for calculating f_0:

$$f_1 - f_0 = 2(f_1 - f_{0.5}) \qquad (32)$$

It is important to note that the values of $f_{0.5}$ and $f_{N+0.5}$ come from the relevant boundary conditions shown in the discretized form in Table 2 available in the Supporting Information. In eqs 20−23, the local velocities at the walls of the volume elements are computed from eq 7 as follows:

$$\bar{v}_{j+0.5} = -\frac{1}{\Delta Z}\frac{4}{150}\left(\frac{\varepsilon}{1 - \varepsilon}\right)^2 r_P^2 \frac{P_0}{\mu v_0 L}(\bar{P}_{j+1} - \bar{P}_j) \qquad (33)$$

The corresponding half-cell approximations for the velocity are given by

$$\bar{v}_{0.5} = \bar{v}|_{Z=0} = -\frac{2}{\Delta Z}\left[\frac{4}{150}\left(\frac{\varepsilon}{1 - \varepsilon}\right)^2\right] r_P^2 \frac{P_0}{\mu v_0 L}(\bar{P}_1 - \bar{P}_{0.5}) \qquad (34)$$

$$\bar{v}_{N+0.5} = \bar{v}|_{Z=1} = -\frac{2}{\Delta Z}\left[\frac{4}{150}\left(\frac{\varepsilon}{1 - \varepsilon}\right)^2\right] r_P^2 \frac{P_0}{\mu v_0 L}(\bar{P}_{N+0.5} - \bar{P}_N) \qquad (35)$$

In cases where the inlet velocity, $\bar{v}_{0.5}$, is known, the half-cell approximation is rearranged to calculate the inlet pressure as follows:

$$\bar{P}_{0.5} = \bar{P}|_{Z=0} = \bar{P}_1 + \frac{\bar{v}_{0.5}\frac{\Delta Z}{2}}{\left[\frac{4}{150}\left(\frac{\varepsilon}{1 - \varepsilon}\right)^2\right] r_P^2 \frac{P_0}{\mu v_0 L}} \qquad (36)$$

In this study, the above system of coupled ordinary differential equations (ODEs) has been solved using ode23s, a stiff ODE solver provided in MATLAB, on a desktop PC with one INTEL Xeon 3.66 GHz CPU and 48.0 GB of RAM.

4. SEPARATION SYSTEM

In this work, the equilibrium-based separation of CO_2 and N_2 on zeolite 13X is considered to illustrate the performance of the finite volume schemes. The equilibrium isotherm data of carbon dioxide and nitrogen on Zeochem zeolite 13X have been gravimetrically measured in our laboratory[38] and fitted to a dual-site Langmuir model:

$$q_i^* = \frac{q_{sb,i}b_i c_i}{1 + \sum_{i=1}^{n_{comp}} b_i c_i} + \frac{q_{sd,i}d_i c_i}{1 + \sum_{i=1}^{n_{comp}} d_i c_i} \qquad (37)$$

where $q_{sb,i}$ and $q_{sd,i}$ are the solid phase saturation loadings of sites 1 and 2, respectively. The parameters b_i and d_i follow the Arrhenius type temperature dependence:

$$b_i = b_{0,i}e^{-\Delta U_{b,i}/RT} \qquad (38)$$

$$d_i = d_{0,i}e^{-\Delta U_{d,i}/RT} \qquad (39)$$

The fitted isotherm parameters are listed in Table 2, and the fitted isotherms at 25 °C are shown in Figure 3.

Table 2. Isotherm Parameters for CO_2/N_2 on Zeochem Zeolite 13X

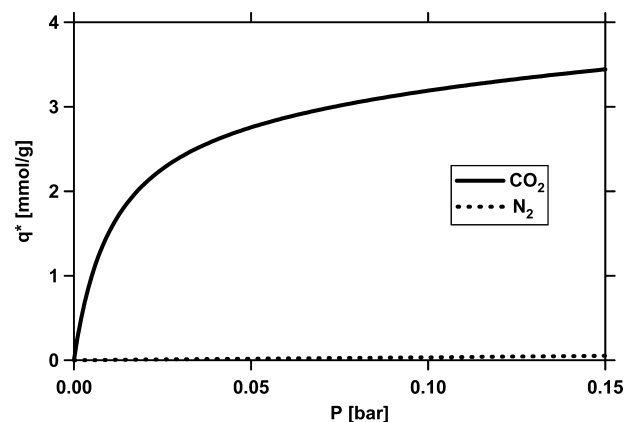| parameter	CO_2	N_2
b_0 [m³ mol⁻¹]	8.65×10^{-7}	2.50×10^{-6}
d_0 [m³ mol⁻¹]	2.63×10^{-8}	0.00
$\Delta U_{b,i}$ [J mol⁻¹]	−36 641.21	-1.58×10^4
$\Delta U_{d,i}$ [J mol⁻¹]	−35 690.66	0.00
$q_{sb,i}$ [mmol g⁻¹]	3.09	5.84
$q_{sd,i}$ [mmol g⁻¹]	2.54	0.00

Figure 3. Single component isotherms of CO_2 and N_2 on Zeochem zeolite 13X at 25 °C.[38]

The transport into the solid phase was assumed to be controlled by molecular diffusion in the macropores. Hence, α_i in eq 3 is given by

$$\alpha_i = k_i \frac{L}{v_0} = \left(\frac{c_i}{q_i^*}\frac{15\varepsilon_p D_p}{r_P^2}\right)\frac{L}{v_0} \qquad (40)$$

where ε_p and r_p correspond to the particle porosity and radius, respectively. D_p is the effective macropore diffusivity, calculated from the following equation:

$$D_p = \frac{D_m}{\tau'} \qquad (41)$$

where D_m is molecular diffusivity and τ' is adsorbent tortuosity. The axial dispersion is calculated using the following:

$$D_L = 0.7D_m + 0.5v_0 d_p \tag{42}$$

where d_p is the diameter of the adsorbent particle.

5. DYNAMIC COLUMN BREAKTHROUGH SIMULATION

As a first case study, the simulation of a dynamic column breakthrough (DCB) experiment is considered. Here, both ends of the column are open and a gas stream is introduced into the bed at $Z = 0$ with a known flow rate. The composition and flow rate are measured at the column outlet using suitable detectors. The pressure at the column outlet is maintained by a back-pressure regulator. This situation is identical to an adsorption step with an open−open boundary condition. This is simulated by fixing the gas velocity, v_{feed}, at the column inlet, and the pressure at the column outlet is assigned to the desired operating pressure. The boundary conditions for breakthrough simulation are listed in Table 2 in the Supporting Information, and the physical properties and operating parameters are listed in Table 3.

In this case study, the column is assumed to be initially saturated with 100% N_2 at $P_H = 1$ bar and a feed containing 15 mol % CO_2 in N_2 is introduced into the column at $Z = 0$. In addition, the column is assumed to be adiabatic ($h_{in} = h_{out} = 0$). Figure 4a shows the breakthrough profiles of y_{CO_2}, $\bar{T}$, and $\bar{v}$ at the column exit simulated using the WENO scheme with 2000 finite volume cells. There are two transitions in Figure 4a.

The first is the sharp transition at $t \sim 520$ s representing the breakthrough of the CO_2 front. The second is around 3600 s, corresponding to the elution of the heat front. The breakthrough of CO_2 is considered complete only after the heat front exits the column. Parts b and c of Figure 4 show the comparison of the composition breakthrough profiles at the two transitions for various numerical schemes using $N = 200$ with the reference (WENO scheme using $N = 2000$). It is shown that all three finite volume schemes are quite close to the reference, while the UDS scheme has significant numerical dispersion. Further, it can be seen that none of the schemes show any spurious oscillations.

At the end of the breakthrough, the amount of CO_2 accumulated inside the column can be computed from a simple mass balance. Then, the mass balance error can be written as

$$J_{MB,DCB}\ (\%) = \frac{\left|(\text{mole}_{in,CO_2} - \text{mole}_{out,CO_2}) - \text{mole}_{acc,CO_2}\right|}{\text{mole}_{acc,CO_2}} \times 100 \tag{43}$$

where

$$\text{mole}_{in,CO_2} = \frac{P_0 v_0}{RT_0}\varepsilon A \int_0^{\tau_{final}} \left[\bar{v}_{0.5}(\tau)\frac{y_{feed}\bar{P}_{0.5}(\tau)}{\bar{T}_{0.5}(\tau)}\right] d\tau \tag{44}$$

$$\text{mole}_{out,CO_2} = \frac{P_0 v_0}{RT_0}\varepsilon A \int_0^{\tau_{final}} \left[\bar{v}_{N+0.5}(\tau)\frac{y_{N+0.5}(\tau)\bar{P}_{N+0.5}(\tau)}{\bar{T}_{N+0.5}(\tau)}\right] d\tau \tag{45}$$

$$\text{mole}_{acc,CO_2} = \int_0^1 \left[\frac{P_0}{RT_0}\varepsilon A\frac{\bar{P}(Z)\,y(Z)}{\bar{T}(Z)}\bigg|_{final} + q_{s,0}(1-\varepsilon)Ax_{final}(Z)\right]dZ$$
$$- \int_0^1 \left[\frac{P_0}{RT_0}\varepsilon A\frac{\bar{P}(Z)\,y(Z)}{\bar{T}(Z)}\bigg|_{initial} + q_{s,0}(1-\varepsilon)Ax_{initial}(Z)\right]dZ \tag{46}$$

In addition to the mass balance error, the energy balance error can be calculated for an adiabatic column from the following equation:

$$J_{EB,DCB}\ (\%) = \frac{\left|\text{heat}_{in} + \text{heat}_{gen} - (\text{heat}_{out} + \text{heat}_{acc,solid} + \text{heat}_{acc,fluid} + \text{heat}_{acc,adsorbed})\right|}{\text{heat}_{out} + \text{heat}_{acc,solid} + \text{heat}_{acc,fluid} + \text{heat}_{acc,adsorbed}} \times 100 \tag{47}$$

where

$$\text{heat}_{in} = \varepsilon A v_0 T_0 C_{p,g}\int_0^{\tau_{final}} \left[\bar{v}_{0.5}(\tau)\,\bar{T}_{0.5}(\tau)\,\rho_{g,0.5}(\tau)\right]d\tau \tag{48}$$

$$\text{heat}_{gen} = (1-\varepsilon)Aq_{i,0}$$
$$\times \int_0^1 \left[\sum_{i=1}^{n_{comp}} -\Delta H_i(x_{i,final}(Z) - x_{i,initial}(Z))\right]dZ \tag{49}$$

$$\text{heat}_{out} = \varepsilon A v_0 C_{p,g}\int_0^{\tau_{final}} \left[\bar{v}_{N+0.5}(\tau)\,\bar{T}_{N+0.5}(\tau)\,\rho_{g,N+0.5}(\tau)\right]d\tau \tag{50}$$

$$\text{heat}_{acc,solid} = (1-\varepsilon)AT_0 C_{p,s}\rho_s\int_0^1 \left[\bar{T}_{final}(Z) - \bar{T}_{initial}(Z)\right]dZ \tag{51}$$

$$\text{heat}_{acc,fluid} = \varepsilon AT_0 C_{p,g}\int_0^1 \left[(\bar{T}(Z)\,\rho_g(Z))_{final}\right.$$
$$\left. - (\bar{T}(Z)\,\rho_g(Z))_{initial}\right]dZ \tag{52}$$

$$\text{heat}_{acc,adsorbed} = (1-\varepsilon)AT_0 q_{i,0}C_{p,a}$$
$$\times \int_0^1 \left\{\sum_{i=1}^{n_{comp}} \left[(\bar{T}(Z)\,x_i(Z))_{final}\right.\right.$$
$$\left.\left. - (\bar{T}(Z)\,x_i(Z))_{initial}\right]\right\}dZ \tag{53}$$

where

Table 3. Parameters Used in Breakthrough and PSA Simulations

parameter	value
column properties	
column length, L [m]	1
inner column radius, r_{in} [m]	0.1445
outer column radius, r_{out} [m]	0.1620
column void fraction, ε	0.37
particle voidage, ε_p	0.35
particle radius, r_p [m]	1.0×10^{-3}
tortuosity, τ'	3
properties and constants	
flue gas pressure, P_f [bar]	1
adsorbent density, ρ_s [kg m^{-3}]	1130
column wall density, ρ_w [kg m^{-3}]	7800
specific heat capacity of gas phase, $C_{p,g}$ [J mol^{-1} K^{-1}]	30.7
specific heat capacity of adsorbed phase, $C_{p,a}$ [J mol^{-1} K^{-1}]	30.7
specific heat capacity of adsorbent, $C_{p,s}$ [J kg^{-1} K^{-1}]	1070
specific heat capacity of column wall, $C_{p,w}$ [J kg^{-1} K^{-1}]	502
fluid viscosity, μ [kg m^{-1} s^{-1}]	1.72×10^{-5}
molecular diffusivity, D_m [m^2 s^{-1}]	1.60×10^{-5}
adiabatic constant, γ	1.4
effective gas thermal conductivity, K_z [J m^{-1} K^{-1} s^{-1}]	0.09
thermal conductivity of column wall, K_w [J m^{-1} K^{-1} s^{-1}]	16
inside heat transfer coefficient, h_{in} [J m^{-2} K^{-1} s^{-1}]	8.6
outside heat transfer coefficient, h_{out} [J m^{-2} K^{-1} s^{-1}]	2.5
universal gas constant, R [m^3 Pa mol^{-1} K^{-1}]	8.314
compression/evacuation efficiency, η	0.72
operating conditions for case studies	
interstitial feed velocity, v_{feed} [m s^{-1}]	1
feed temperature, T_{feed} [K]	298.15
ambient temperature, T_a [K]	298.15
high pressure, P_H [bar]	1
intermediate pressure, P_I [bar]	0.2
low pressure, P_L [bar]	0.1
constants for dimensionless parameters	
P_0 [bar]	P_H
T_0 [K]	T_{feed}
v_0 [m s^{-1}]	v_{feed}
$q_{s,0}$ [mmol g^{-1}]	$q_{sb,\,N_2}$

$$\rho_{g,j}(\tau) = \frac{P_0}{T_0} \frac{\overline{P}_j(\tau)}{R\overline{T}_j(\tau)} \tag{54}$$

The energy and mass balance errors for the four schemes are shown in Figure 5. As expected, the error decreases with increasing N. All schemes have comparable energy and mass balance errors for the same number of cells, and the errors are always less than 2% for the mass balance and 0.4% for the energy balance.

A systematic study to understand the effect of N on the performance of different schemes is carried out by using the L_1 norm. The L_1 norm for a state variable, f, is defined as

$$L_{1,f} = \frac{\sum_{i=1}^{n_t} |f_{ref,t} - f_t| \Delta t}{\sum_{i=1}^{n_t} f_{ref,t} \Delta t} \tag{55}$$

The breakthrough profile using WENO with $N = 2000$ is used as a reference. The denominator in eq 55 helps to ensure that the comparison of the three state variables (composition,

temperature, and pressure) are on the same scale. The total L_1 is defined as

$$L_1 = L_{1,y} + L_{1,T} + L_{1,P} \tag{56}$$

The effects of N on the convergence error for the four schemes are shown in Figure 6a. The convergence of each scheme is indicated alongside each curve. It can be seen that UDS has a lower convergence compared to the finite volume schemes. It can also be seen that WENO has the highest convergence with an average slope of 1.56. When considering the L_1 norms, Superbee has the lowest values for $N \leq 100$, but its convergence of 1.21 is the least among the three finite volume schemes. For $N > 100$, van Leer and WENO perform better than Superbee in terms of the L_1 norm.

From a practical perspective, it is important to understand the trade-off between accuracy and computational time. Figure 6b provides some indications for choosing a suitable numerical scheme for a desired accuracy. Although the mass and energy balance errors for the four schemes are comparable for any N (cf. Figure 5), the computational time required for each scheme is very different for a given N. Figure 6b shows that, for low L_1 norms, WENO is at least 2 orders of magnitude faster than the others. However, van Leer is nearly as fast as WENO in the low accuracy region ($N < 30$). Superbee is slower because of the min/max function evaluations that occur in its flux limiter. In section 6, we will evaluate the performance of the numerical schemes using a four-bed cyclic adsorption process.

6. PROCESS SIMULATION

In section 5, the performances of various numerical schemes were evaluated for simulating a dynamic column breakthrough experiment. In this section, the evaluation is extended to a cyclic adsorption process. First, in section 6.1 we describe a four-step process for CO_2 capture in detail and analyze its simulation results. Then, in section 6.2, we compare the performance of various numerical schemes.

6.1. Four-Step VSA for CO_2 Capture. A four-step VSA cycle process, shown in Figure 7, is chosen as a case study for further evaluation of the numerical schemes. The process consists of the following steps:

1. Feed Pressurization: The feed containing 15 mol % CO_2 and 85 mol % N_2 at 1 bar and 25 °C (representative of dry, postcombustion flue gas from a coal-fired power plant) is introduced into the column from the feed end ($Z = 0$). The other end of the column ($Z = 1$) is closed and the column pressure is raised to P_H. Note that in a VSA process $P_H = 1$ bar. The pressurization profile at $Z = 0$ is assumed to obey the following functional form:

$$\overline{P}_{0.5} = \overline{P}|_{Z=0} = \frac{1}{P_0}(P_H - (P_H - P_L)e^{-\lambda \tau L/v_0}) \tag{57}$$

2. High Pressure Adsorption: The feed continues to enter the column, and the light-product end ($Z = 1$) is opened. CO_2, the heavier component, is preferentially adsorbed and N_2-rich raffinate is collected from the light-product end.

3. Blowdown: The feed end is closed and the column pressure is reduced to an intermediate pressure, $P_I < 1$ bar, by pulling vacuum at $Z = 1$. The aim of this step is to remove as much N_2 as possible, while retaining CO_2 in the column for recovery in the next step. The depressurization profile at $Z = 1$ is set to obey the following functional form:
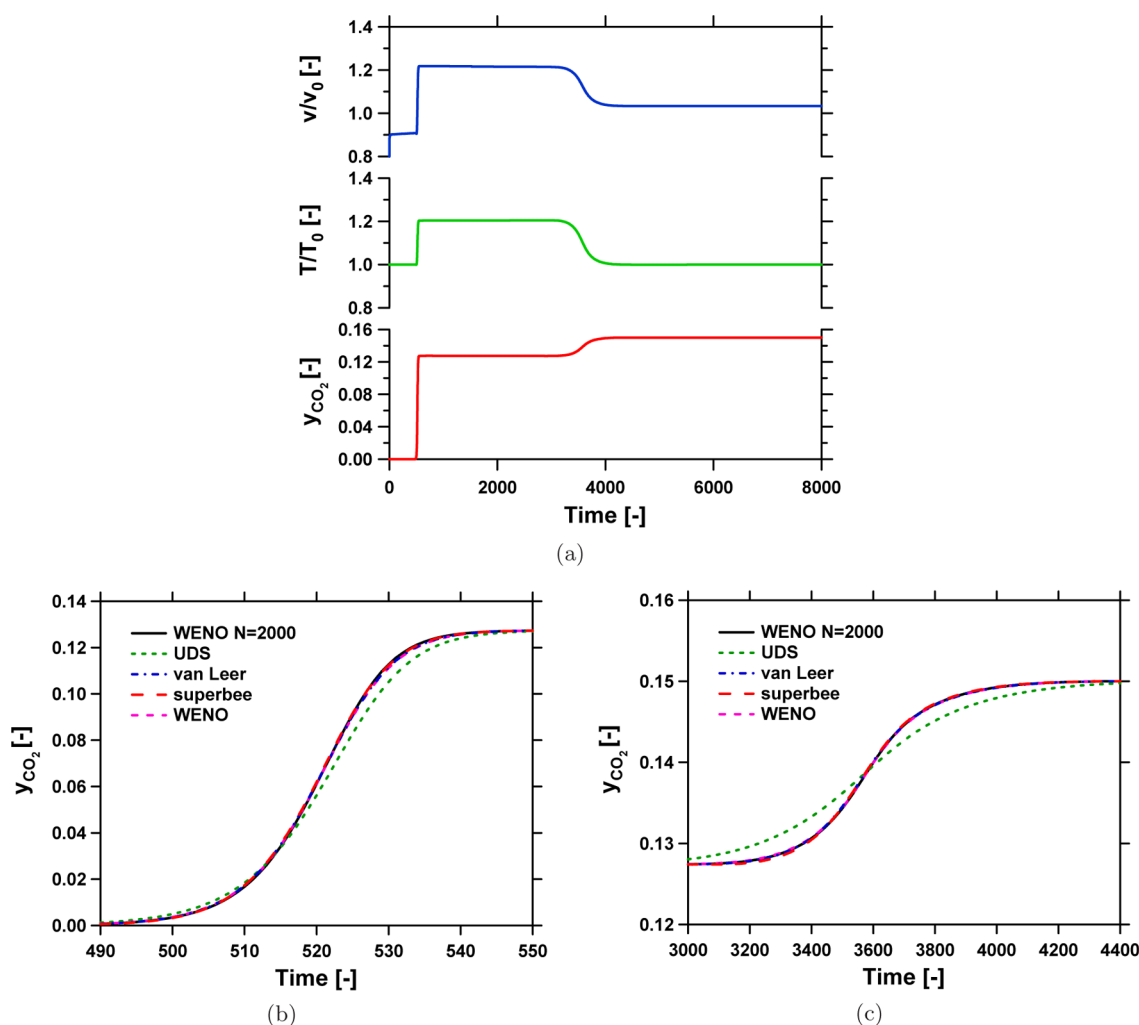
Figure 4. Composition, temperature, and velocity breakthrough profiles for CO_2 at the exit of the adsorption column. (a) Simulated with 2000 discretization volumes using WENO scheme. (b, c) Comparison of composition breakthrough profiles at the two transitions for different numerical schemes with $N = 200$.
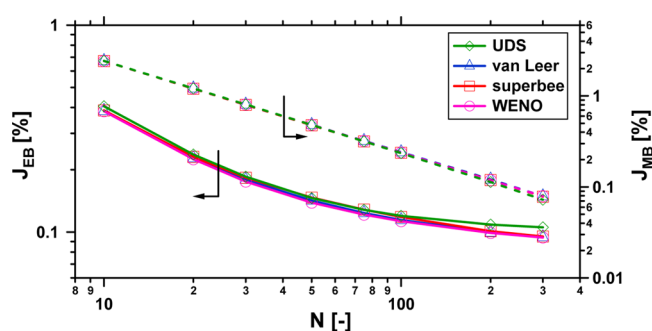

Figure 5. Effect of number of volume elements on the energy balance and mass balance errors for the case study on dynamic column breakthrough. Solid lines represent energy balance errors, and dotted lines represent mass balance errors.

$$\overline{P}_{N+0.5} = \overline{P}|_{Z=1} = \frac{1}{P_0}(P_I + (P_H - P_I)e^{-\lambda\tau L/v_0})$$
(58)

4. Evacuation: The light-product end is closed and enriched CO_2 product is collected from the feed end by decreasing the column pressure to P_L ($P_L < P_I < 1$ bar). The depressurization profile at $Z = 0$ is set as follows:

$$\overline{P}_{0.5} = \overline{P}|_{Z=0} = \frac{1}{P_0}(P_L + (P_I - P_L)e^{-\lambda\tau L/v_0})$$
(59)

The specific operating parameters for each step of the cycle are listed in Table 4. The physical properties and the parameters used in this study are the same as in Table 3. The boundary conditions for each step are listed in Table 2 in the Supporting Information. At the start of the simulation, the column is considered to be saturated with 100% N_2 at P_L. The state of the column at the end of a step is taken as the initial condition for the subsequent step. The sequence of steps is repeated until a cyclic steady state (CSS) is reached. Strictly, a CSS condition is reached when there is no change in the column profiles of all state variables after each step for two consecutive cycles. The performance of the process is evaluated by considering CO_2 purity and recovery at CSS, which are defined as

$$\text{purity (\%)} = \left[\frac{\text{mole}_{\text{out},CO_2}|_{\text{evac}}}{\text{mole}_{\text{out},CO_2}|_{\text{evac}} + \text{mole}_{\text{out},N_2}|_{\text{evac}}}\right] \times 100$$
(60)

$$\text{recovery (\%)} = \left[\frac{\text{mole}_{\text{out},CO_2}|_{\text{evac}}}{\text{mole}_{\text{in},CO_2}|_{\text{press}} + \text{mole}_{\text{in},CO_2}|_{\text{ads}}}\right] \times 100$$
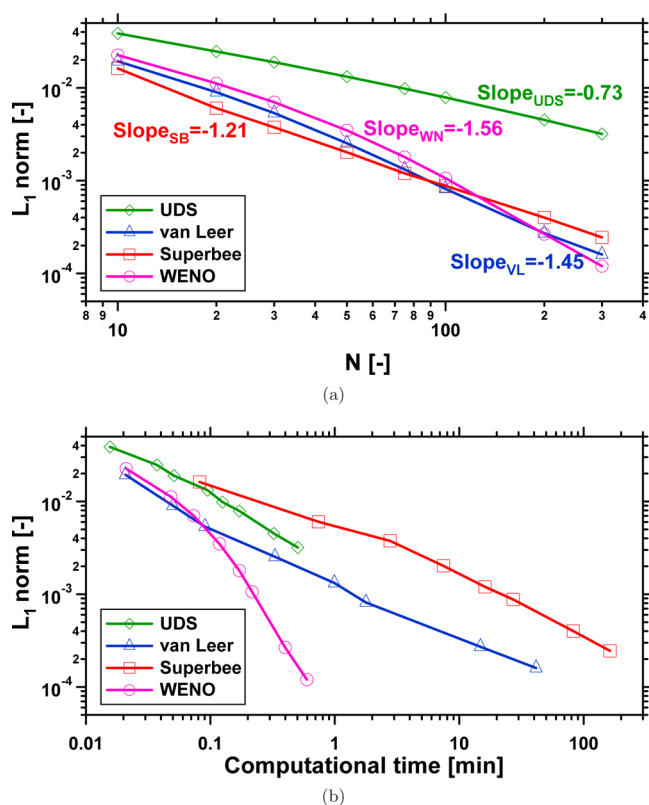(61)

(a)

(b)

Figure 6. Results from the case study of dynamic column breakthrough. (a) Convergence plot. (b) L_1 norm versus computational time. For each method, the symbols represent discretization volumes of 10, 20, 30, 50, 75, 100, 200, and 300 in the direction of decreasing L_1 norm.
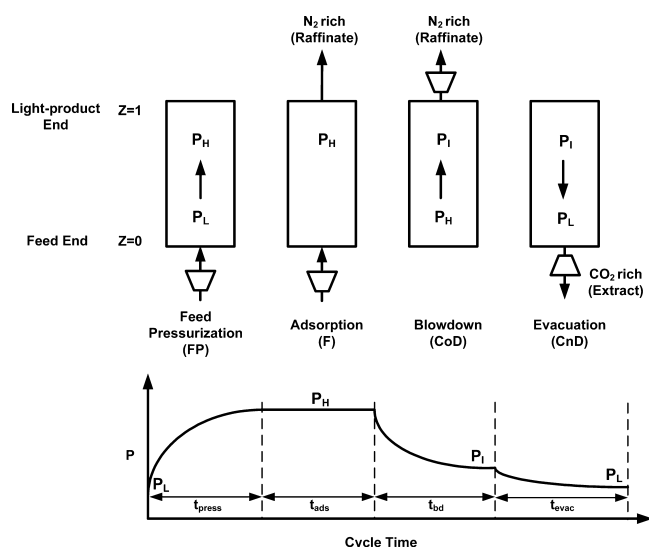

Figure 7. The four-step cycle for CO_2 capture.

where

$$\text{mole}_{\text{in,CO}_2} = \frac{P_0 v_0}{RT_0}\varepsilon A \int_0^{\tau_{\text{step}}} \left[\bar{v}_{0.5}(\tau)\frac{y_{0.5}(\tau)\,\bar{P}_{0.5}(\tau)}{\bar{T}_{0.5}(\tau)}\right]d\tau \tag{62}$$

$$\text{mole}_{\text{out,CO}_2} = \frac{P_0 v_0}{RT_0}\varepsilon A \int_0^{\tau_{\text{step}}} \left[\bar{v}_{N+0.5}(\tau)\frac{y_{N+0.5}(\tau)\,\bar{P}_{N+0.5}(\tau)}{\bar{T}_{N+0.5}(\tau)}\right]d\tau \tag{63}$$

Table 4. Specific Parameters for Each Step in the Four-Step PSA Simulation

step	feed and operating conditions
pressurization	$t_{\text{press}} = 15$ s, $y_{\text{feed,CO}_2} = 0.15$, $\lambda = 0.5$ s^{-1}, $P_L = 0.1$ bar $\rightarrow$ $P_H = 1.0$ bar
adsorption	$t_{\text{ads}} = 15$ s, $y_{\text{feed,CO}_2} = 0.15$, $v_{\text{feed}} = 1$ m s^{-1}, $P_H = 1.0$ bar
forward blowdown	$t_{\text{bd}} = 30$ s, $\lambda = 0.5$ s^{-1}, $P_H = 1.0$ bar $\rightarrow$ $P_I = 0.2$ bar
reverse evacuation	$t_{\text{evac}} = 40$ s, $\lambda = 0.5$ s^{-1}, $P_I = 0.2$ bar $\rightarrow$ $P_L = 0.1$ bar

$$\text{mole}_{\text{out,CO}_2}\big|_{\text{evac}} = \frac{P_0 v_0}{RT_0}\varepsilon A \int_0^{\tau_{\text{evac}}} \left[\bar{v}_{0.5}(\tau)\frac{y_{0.5}(\tau)\,\bar{P}_{0.5}(\tau)}{\bar{T}_{0.5}(\tau)}\right]d\tau \tag{64}$$

Results from the WENO scheme with $N = 1000$ yield CO_2 purity and recovery of 88.74% and 35.83%, respectively. The internal column profiles of y, x, and $\bar{T}$ at the end of each step are shown in Figure 8. The high purity can be rationalized by considering the high feed velocity during the adsorption step and the high capacity of zeolite 13X for CO_2 (cf. Figure 8b). The low recovery can be explained by considering the gas phase CO_2 compositions at the completion of the adsorption and blowdown steps in Figure 8c. It can be seen that the CO_2 front reaches the light-product end of the column at the end of the adsorption step. Due to this, CO_2 is lost along with nitrogen during the blowdown step, resulting in a low recovery. Recall that the main role of the blowdown step is to remove as much N_2 as possible in order to prevent the contamination of the CO_2 product. However, in the present case this resulted in CO_2 loss, which should be avoided in order to increase recovery. Clearly, a full optimization of the various operating parameters of the process is essential to obtaining the desired purity and recovery, which will be addressed in section 7.1.

6.2. Comparison of Numerical Schemes. Having described the performance of the simulator, the next step is to compare the performance of various schemes. For this, we consider WENO with $N = 1000$ as the reference. It is also worth pointing out that all simulations were performed up to 500 cycles to ensure the attainment of CSS. For full optimization, it would be desirable to use the fastest scheme with sufficient accuracy. The choice of N obviously plays a critical role in deciding these characteristics. Therefore, the effect of N on CO_2 purity and recovery and also the computational time for different numerical schemes were studied, and the results are shown in Figure 9. It is clear from Figure 9a that, for all the finite volume schemes, purity and recovery for $N \geq 30$ are close to the reference values. On the other hand, the purity and recovery for UDS are lower than the reference values for $N < 100$. These results indicate that for $N \geq 30$ with any finite volume scheme offers sufficient accuracy. Having fixed N, we now compare the finite volume schemes in terms of computational speed. As seen from Figure 9b, WENO and van Leer are faster for $N \leq 30$, but WENO is the clear choice for $N > 30$. Thus, we will use WENO with $N = 30$ to demonstrate its effectiveness in optimizing the four-step cycle for CO_2 capture.

7. OPTIMIZATION OF A FOUR-STEP CYCLE FOR CO_2 CAPTURE

Any separation process for CO_2 capture must satisfy regulatory stipulations; i.e., CO_2 purity and recovery should be in excess of 90%.[39] Furthermore, the energy required for CCC in a power plant, called the "parasitic energy" or "energy penalty", must be minimized, as it reduces the plant's net electricity output. Besides the energy consumption, the size of the CCC plant is
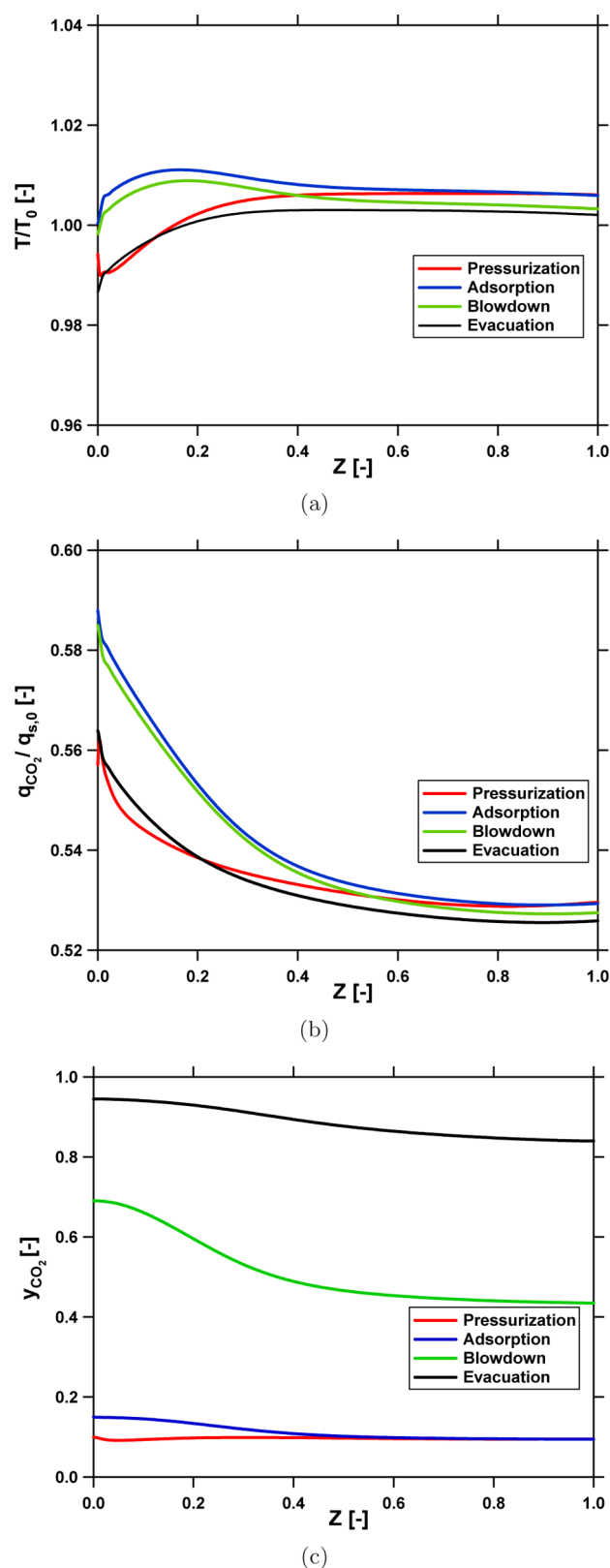
Figure 8. Cyclic steady state (n_{cycle} = 500) gas and solid phase column profiles at the end of each step for WENO with 1000 volume elements.

Figure 9. (a) Convergence of CO_2 purity and recovery for different numerical schemes. (b) Computational time required at different discretization volumes for each numerical scheme. The symbols from left to right represent discretization volumes of 10, 20, 30, 50, 75, 100, 200, and 300.

also an important consideration. This is especially true given the large volume of CO_2 emissions. Hence, for any separation technology to be economically competitive, it must use minimum parasitic energy (or energy penalty) and have maximum
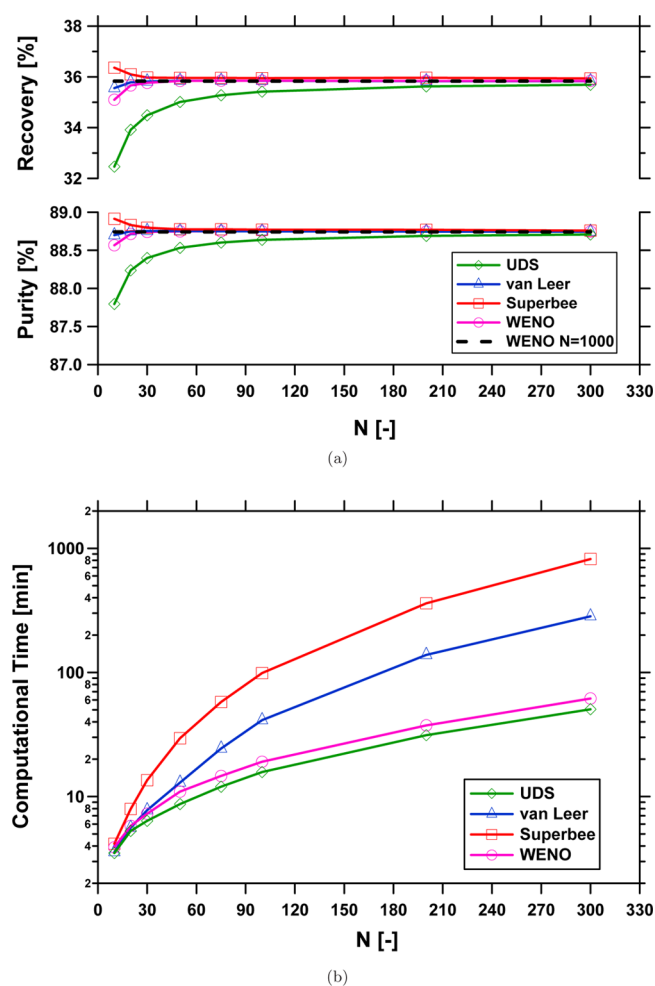
productivity. Owing to the transient and complex nature of adsorption processes and the nontrivial interplay of their operating parameters, very few reported processes have achieved the 90% purity−recovery demand. In this study, we consider postcombustion CCC for a coal based power plant using Zeochem zeolite 13X as an adsorbent. We perform rigorous optimization of a four-step cycle to identify operating conditions at which the purity and recovery demands can be met and to compute the energy penalty and productivity of the process. Since these goals involve competing objectives, e.g., maximizing purity and recovery and maximizing productivity and minimizing energy consumption, we consider multiple objectives during optimization. To this end, we use the compositions and conditions from section 6 and Table 4 and employ the nondominated sorting genetic algorithm II (NSGA-II), available in the MATLAB global optimization toolbox. In all the optimization problems, the number of the population was equal to $10n_{DV}$, where n_{DV} is the number of decision variables, and the genetic algorithm was run up to 60 generations. In this work, one optimization runs means a full two-objective Pareto solution. This takes 1 day of wall time. This also closely approximates the CPU time, as we use a dedicated computer. A mass balance error of less than 0.5% for five consecutive cycles is specified as the criterion for attainment of CSS.

Table 5. Lower and Upper Bounds for Decision Variables in the Optimization Problem of Four-Step VSA and PVSA Cycle

cycle	t_{ads} [s]	t_{bd} [s]	t_{evac} [s]	P_H [bar]	P_I [bar]	P_L [bar]	v_{feed} [m s^{-1}]
four-step VSA	20−100	30−200	30−200	fixed at 1	0.05−0.5	0.05−0.5	0.1−2
four-step PVSA	20−100	30−200	30−200	1−10	0.13−3	0.13−0.5	0.1−2

7.1. Maximization of Purity−Recovery. A four-step cycle has eight operating parameters, namely, the durations of the four steps (t_{press}, t_{ads}, t_{bd}, t_{evac}), three operating pressures (P_H, P_I, P_L), and the inlet feed velocity (v_{feed}) in the high pressure adsorption step. Of these eight parameters, the duration of the pressurization step has been fixed at 20 s, since a shorter duration is unrealistic in industrial scale operation and a longer duration has negligible effect on process performance. Among the remaining seven parameters, the decision variables for optimization are chosen based on the objectives and the cycle under study. In the following, two operating scenarios, first the pure VSA cycle and then the PVSA cycle, are considered.

7.1.1. VSA Process. In this process, the column exit during the high pressure adsorption step is fixed at 1 bar, while the blowdown and evacuation steps are performed at different vacuum levels. This leaves six decision variables for optimization, namely, t_{ads}, t_{bd}, t_{evac}, P_I, P_L, and v_{feed}. The bounds for all decision variables are listed in Table 5. In order to ensure that the blowdown and evacuation pressures are unequal, the following constraint is used.

$$P_I \geq P_L + 0.01 \text{ [bar]} \qquad (65)$$

From Figure 3, the highly nonlinear shape of the CO_2 isotherm is obvious. Hence, it can be envisaged that very low vacuum pressure will be required to achieve the 90% purity−recovery target. Because the evacuation pressure is an important design variable, its impact on the process performance was studied using four optimization runs to maximize purity and recovery simultaneously. The lower bounds of P_L for the four runs were specified as 0.05, 0.03, 0.02, and 0.01 bar respectively, keeping t_{ads}, t_{bd}, t_{evac}, P_I, and v_{feed} as decision variables. After the optimization runs, the nondominated points were plotted as the four Pareto curves shown in Figure 10a. In other words, moving from one point on any Pareto curve to another on the same curve results in the improvement of one objective at the expense of the other. Furthermore, each point on a Pareto curve corresponds to a unique set of six decision variable values. Thus, each Pareto curve offers a range of trade-offs between two objectives, from which the operator can select a desired operating point. From Figure 10a, as expected, it can be seen that the purity−recovery performance improves as the evacuation pressure decreases. It can be also seen that an evacuation pressure of $P_L \leq 0.02$ bar or lower is required to achieve ≥90% purity−recovery.

The values of P_I and P_L for the Pareto curve corresponding to $P_L \geq 0.01$ bar are shown in Figure 11. From Figure 11b, it can be seen that evacuation pressures near their lower bounds are required to maximize purity and recovery. Figure 11a shows clearly the effect of the blowdown pressure on product purity. Lower blowdown pressures increase product purity but decrease recovery. The plots also indicate that operating the unit at a low P_I allows removal of significant amounts of N_2 from the column, thereby resulting in a high CO_2 purity. However, a significant amount of CO_2 is lost in the blowdown gas, which contributes to the low CO_2 recovery.

7.1.2. PVSA Process. As discussed earlier, in this process we consider the operation of the high pressure adsorption step above atmospheric pressures. Hence, P_H is no longer fixed and
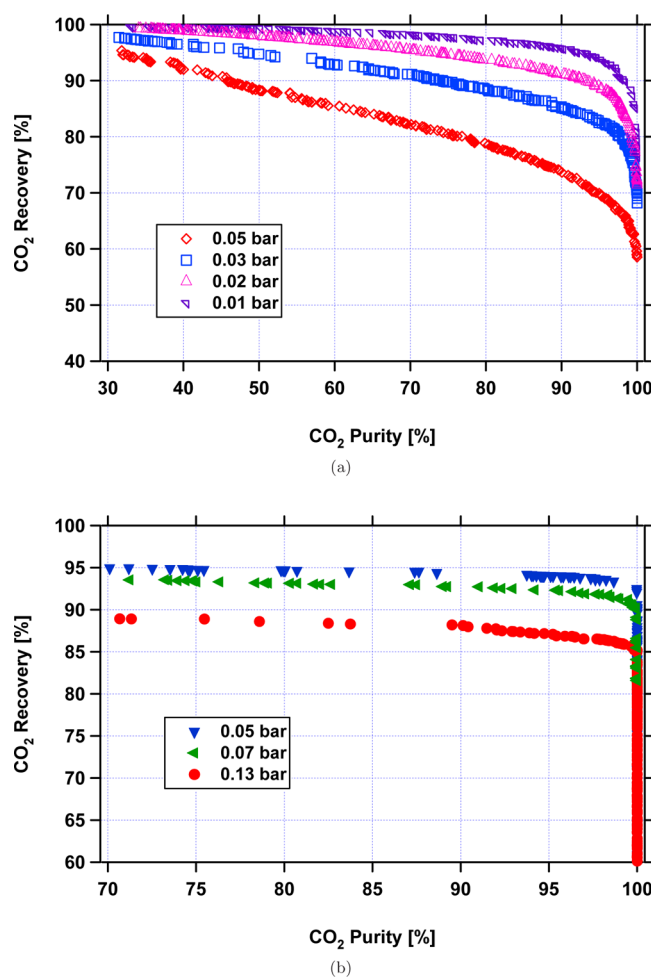

(a)

(b)

Figure 10. Pareto curves for the optimization problem of simultaneously maximizing purity and recovery. (a) VSA cycle; each case was generated by changing the lower bound of P_L to the value provided in the legend. (b) PVSA cycle; each case was generated by changing the evacuation pressure to the value provided in the legend.

becomes a decision variable between 1 and 10 bar. The blowdown step can be performed at either above or below atmospheric pressures, while the evacuation step is always performed at subatmospheric pressures. Thus, we have t_{ads}, t_{bd}, t_{evac}, P_H, P_I, P_L, and v_{feed} as seven decision variables. An evacuation pressure of $P_L = 0.02$ bar may be difficult to achieve in a real plant. Hence, to obtain the purity−recovery target, either the feed pressure should be increased or alternative cycles should be examined. We explore the former possibility here while the latter is considered in a follow-up paper. While P_H beyond 10 bar can be achieved in practice, it is not considered here due to adverse energy impact. In this study, three cases of $P_L \geq 0.13$ bar, $P_L \geq 0.07$ bar, and $P_L \geq 0.05$ bar are considered. The Pareto curves for these cases are presented in Figure 10b. Although Zeochem zeolite 13X shows high CO_2/N_2 selectivity, achieving high purity−recovery simultaneously is challenging and requires vacuum evacuation despite pressurizing the feed to a higher pressure.
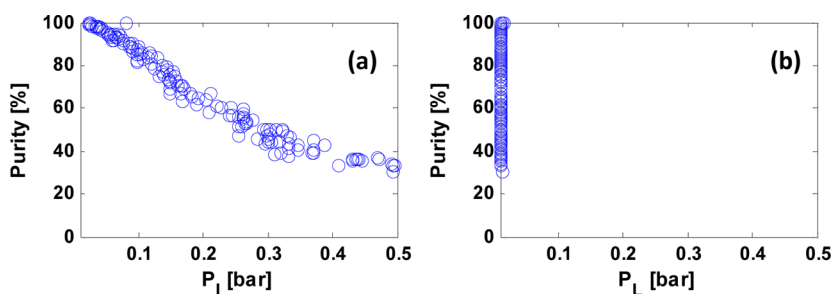
Figure 11. (a) Blowdown and (b) evacuation pressures corresponding to the Pareto front in Figure 10a for the four-step VSA cycle with the lower bound of P_L equal to 0.01 bar.

7.2. Minimization of Energy and Maximization of Productivity.

Once a process is shown to satisfy the 90% purity–recovery constraint, it is important to compute its energy need and productivity. The VSA process can be considered as a special case of the PVSA process with $P_H = 1$ bar; hence we consider the optimization of the PVSA process only. In this work, we use P_f to denote flue gas pressure and assume that all vacuum pumps discharge at 1 bar. In the PVSA process, energy may be consumed in all four steps. During the pressurization step, the pressure increases from P_L to P_H. If $P_H > P_f$, then no energy is required to take the column from P_L to P_f, while compression is required to take it from P_f to P_H. During the adsorption step, if

$P_H = P_f$, then energy is required only to overcome the frictional pressure drop in the column. However, if $P_H > P_f$, then energy is required to compress the feed gas from P_f to P_H. Similarly, the blowdown step may be performed at any pressure between P_H and P_L. Thus, the pressure decreases from P_H to P_I in this step. If $P_I > 1$ bar, then the blowdown step does not require any energy. However, if $P_I < 1$ bar, then energy is required only to evacuate from 1 bar to P_I. A similar argument holds for the evacuation step, where the pressure decreases from P_I and P_L. If $P_I > 1$ bar, then energy is required only to evacuate from 1 bar to P_L. If $P_I < 1$ bar, then energy is required to evacuate from P_I and P_L. Therefore, the energy consumption for each step is calculated as follows:

$$E_{press} = \begin{cases} \dfrac{1}{\eta} \varepsilon \pi r_{in}^2 v_0 P_0 \dfrac{\gamma}{\gamma - 1} \int_{t=0}^{t=t_{press}} (\bar{v}\bar{P}|_{Z=0}) \left[\left(\dfrac{P_0 \bar{P}|_{Z=0}}{P_f} \right)^{(\gamma-1)/\gamma} - 1 \right] dt & \text{if } P|_{z=0} > P_f \\ \\ 0 & \text{if } P|_{z=0} \leq P_f \end{cases} \tag{66}$$

$$E_{ads} = \dfrac{1}{\eta} \varepsilon \pi r_{in}^2 v_0 P_0 \dfrac{\gamma}{\gamma - 1} \int_{t=0}^{t=t_{ads}} (\bar{v}\bar{P}|_{Z=0}) \left[\left(\dfrac{P_0 \bar{P}|_{Z=0}}{P_f} \right)^{(\gamma-1)/\gamma} - 1 \right] dt \tag{67}$$

$$E_{bd} = \begin{cases} \dfrac{1}{\eta} \varepsilon \pi r_{in}^2 v_0 P_0 \dfrac{\gamma}{\gamma - 1} \int_{t=0}^{t=t_{bd}} (\bar{v}\bar{P}|_{Z=1}) \left[\left(\dfrac{P_{atm}}{P_0 \bar{P}|_{Z=1}} \right)^{(\gamma-1)/\gamma} - 1 \right] dt & \text{if } P|_{z=L} < 1 \text{ bar} \\ \\ 0 & \text{if } P|_{z=L} \geq 1 \text{ bar} \end{cases} \tag{68}$$

$$E_{evac} = \dfrac{1}{\eta} \varepsilon \pi r_{in}^2 v_0 P_0 \dfrac{\gamma}{\gamma - 1} \int_{t=0}^{t=t_{evac}} (\bar{v}\bar{P}|_{Z=0}) \left[\left(\dfrac{P_{atm}}{P_0 \bar{P}|_{Z=0}} \right)^{(\gamma-1)/\gamma} - 1 \right] dt \tag{69}$$

where $P_{atm} = 1$ bar, η is the compression efficiency, and γ is the adiabatic constant. In this section P_f is taken as 1 bar, $\eta = 0.72$, and $\gamma = 1.4$ in all energy calculations. The

total energy consumption in terms of kilowatt hours per metric ton of CO_2 captured is calculated by the following equation:

$$E_T \left[\frac{kWh}{t \text{ of } CO_2 \text{ captured}} \right]$$

$$= \frac{E_{press} + E_{ads} + E_{bd} + E_{evac}}{\text{mass of } CO_2 \text{ in the extract stream(s) per cycle}} \quad (70)$$

Productivity is calculated as

$$\text{productivity} \left[\frac{mol}{m^3 \text{ adsorbent} \cdot s} \right]$$

$$= \frac{mole_{out,CO_2}\big|_{evac}}{(\text{total volume of the adsorbent})(\text{cycle time})} \quad (71)$$

The decision variables for energy-productivity optimization in this section are t_{ads}, t_{bd}, t_{evac}, P_I, P_H, and v_{feed} and their ranges are listed in Table 5. We consider seven levels of fixed evacuation pressure, namely, 0.005, 0.01, 0.02, 0.03, 0.05, 0.07, and 0.1 bar. Finally, all the optimization runs are performed by employing the constraints of purity ≥90% and recovery ≥90%, which are incorporated by penalizing each objective function.

Figure 12 shows energy−productivity Paretos for P_L = 0.02, 0.03, 0.05, 0.07, and 0.1 bar. It is seen that, by pressurizing the feed, it is
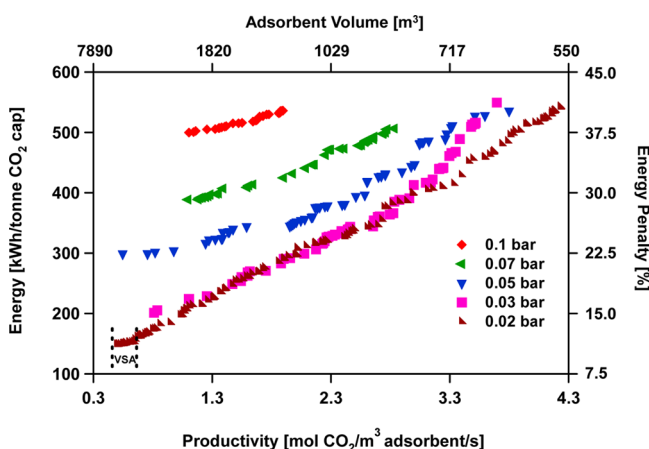

Figure 12. Pareto curves for the maximization of productivity and minimization of energy for the four-step PVSA cycle. Each curve is the result of optimization for a fixed evacuation pressure specified in the legend. Excepting the small segment marked as VSA for P_L = 0.02 bar, all other Pareto points involved feed pressurization in order to meet purity−recovery requirement.

possible to achieve the target purity and recovery at evacuation pressure as high as ~0.1 bar. In addition, the Pareto curves for higher values of P_L are shorter compared to those at lower pressure. This can be rationalized by the fact that at high values of P_L the operating space where the constraints are met is rather limited compared to the lower values of P_L. Further, for a given energy consumption, productivity increases with decreasing evacuation pressure. On the other hand, for a given productivity, the energy consumption decreases with decreasing evacuation pressure. In order to render a practical perspective, energy consumption and productivity are also expressed as energy penalty and adsorbent volume for a 500 MW coal based power plant emitting 10 000 t of CO_2/day, and shown on the secondary axes in Figure 12. Parasitic energy is defined as

$$\text{parasitic energy or energy penalty}$$

$$= \frac{\text{energy required for } CO_2 \text{ capture}}{\text{energy produced by power plant}} \quad (72)$$

Except for the small segment marked as VSA for P_L = 0.02 bar, all other Pareto points involved feed pressurization in order to meet the purity−recovery requirement.

In order to understand the contribution of the different steps to the total energy consumption, we consider the point on each Pareto curve with the lowest energy consumption. The operating conditions corresponding to these minimum energy points are listed in Table 6. In Figure 13, the contribution from the pressurization and adsorption steps and that from the blowdown and evacuation steps are shown separately. The optimal P_H values corresponding to the minimum energy consumption are also plotted. Clearly, for $P_L \leq 0.02$ bar, $P_H = 1$ bar; i.e., a VSA process is sufficient to meet regulatory targets. In this range, the total energy consumption is purely from the blowdown and evacuation steps, which decreases with increasing P_L. For $P_L > 0.02$ bar, the optimization results reveal that the purity−recovery constraint is met only by pressurizing the feed, i.e., a PVSA process. Further, increasing P_L beyond 0.02 bar also requires increasing P_H in order to meet the purity−recovery constraint. Hence, for $P_L > 0.02$ bar, the total energy consumption involves both pressurization and evacuation. While the energy consumption for evacuation decreases with increasing P_L, that for the corresponding pressurization increases. There is a clear minimum in the total energy consumption with respect to P_L, and this corresponds to the pressure at which the optimal process transitions from a pure VSA to a PVSA mode of operation. Therefore, pressurizing the feed gas for CCC is energetically unfavorable.

Clearly, the minimum energy penalty for CCC using the four-step cycle investigated here is 11%. Although pressurizing the feed flue gas stream can be prohibitively energy intensive, it nevertheless provides the following advantages. First, it allows meeting the CO_2 purity−recovery target without resorting to deep vacuum in a four-step cycle. Second, it offers higher productivity at the expense of a higher energy penalty, which is important for reducing the plant size. As mentioned before, plant size is a critical consideration for CCC units, particularly for retrofitting existing power plants.

Table 6. Operating Conditions Corresponding to Minimum Energy for Four-Step PVSA Cycle at Different Evacuation Pressures

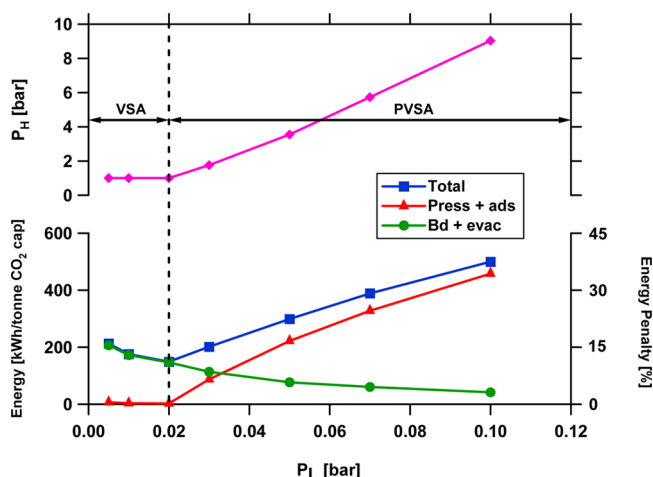| case	t_{ads} [s]	t_{bd} [s]	t_{evac} [s]	P_I [bar]	P_H [bar]	v_{feed} [m s⁻¹]	total energy [kWh t⁻¹]
P_L = 0.005 bar	89.55	34.54	120.7	0.26	1.00	0.91	213.22
P_L = 0.01 bar	80.24	54.05	101.83	0.22	1.00	0.86	176.14
P_L = 0.02 bar	94.89	122.84	189.46	0.18	1.00	0.58	148.96
P_L = 0.03 bar	69.36	30.95	124.27	0.22	1.76	0.41	201.50
P_L = 0.05 bar	91.63	161.32	195.24	0.43	3.54	0.19	298.92
P_L = 0.07 bar	70.93	54.13	88.45	0.53	5.73	0.15	388.68
P_L = 0.1 bar	97.36	94.52	128.45	1.07	9.04	0.11	499.65

Figure 13. Effect of evacuation pressure on minimum energy consumption for four-step PVSA cycle. The figure on the top shows the corresponding P_H required to meet purity–recovery constraints for every fixed value of P_L.

8. CONCLUSIONS

A fast, robust, and flexible simulator has been developed, which can simulate a variety of PVSA processes using a detailed non-isothermal and nonisobaric model. It uses a finite volume scheme, and it has been successfully used for GA-based detailed optimization of a four-step PVSA cycle for CO_2 capture and concentration on Zeochem zeolite 13X from a 15% mixture in N_2, representative of dry, postcombustion flue gas from a coal fired power plant. The study has led to the following conclusions:

1. Two high-resolution TVD schemes, namely van Leer and Superbee, and a finite volume scheme, WENO, have been compared along with full implementation details. The trade-off plots of error versus computational speed show that 30 volume elements are sufficient to achieve the desirable accuracy of the process performance indicators, such as purity and recovery, and the WENO scheme is computationally the most efficient among the three.

2. When operating pressures are allowed to vary from 0.01 to 10 bar, the energy required by the four-step PVSA cycle to achieve 90% purity–recovery constraint is the minimum, when it operates in the VSA mode with $P_L = 0.02$ bar. This minimum energy is 149 kWh/t of CO_2 captured at a productivity of 0.49 mol of CO_2/m^3 of adsorbent/s, which is equivalent to an energy penalty of 11%. This suggests that pressurizing the feed in a four-step cycle is not favorable, as far as the energy penalty is concerned.

3. If a higher P_L is desired in this four-step PVSA cycle, then the feed must be pressurized in order to meet the purity–recovery constraint. Although energetically unfavorable, pressurizing the feed while maintaining P_L in the range 0.02–0.03 bar allows up to 8-fold increase in productivity with energy consumption increasing at approximately half that rate. Therefore, a combination of feed pressurization and low P_L offers the possibility of significant reduction in plant size and capital cost, although at the expense of the energy penalty.

■ APPENDIX

A.1. Dimensional Form of the Model Equations

The component mass balance is given by

$$\frac{\partial c_i}{\partial t} = -\frac{\partial}{\partial z}\left[c D_L \frac{\partial y_i}{\partial z} + c_i v\right] - \frac{1-\varepsilon}{\varepsilon}\frac{\partial q_i}{\partial t} \tag{A.1}$$

where c_i and q_i are the fluid and solid phase concentrations of component i, respectively, D_L is the coefficient of axial dispersion, v is the interstitial velocity in the axial direction, c is the total concentration, y_i is the mole fraction in the fluid phase, and z is the axial distance. By using the ideal gas law, eq A.1 can be written as

$$\frac{\partial y_i}{\partial t} + \frac{y_i}{P}\frac{\partial P}{\partial t} - \frac{y_i}{T}\frac{\partial T}{\partial t}$$
$$= \frac{T}{P}D_L\frac{\partial}{\partial z}\left(\frac{P}{T}\frac{\partial y_i}{\partial z}\right) - \frac{T}{P}\frac{\partial}{\partial z}\left(\frac{y_i P}{T}v\right) - \frac{RT}{P}\frac{1-\varepsilon}{\varepsilon}\frac{\partial q_i}{\partial t} \tag{A.2}$$

The space derivative terms are not expanded for the convenience of uniformly implementing the finite volume schemes. Adding the component mass balance equations, given by eq A.2 for component i, subject to the conditions $\sum y_i = 1$, the following total mass balance equation is obtained:

$$\frac{1}{P}\frac{\partial P}{\partial t} - \frac{1}{T}\frac{\partial T}{\partial t} = -\frac{T}{P}\frac{\partial}{\partial z}\left(\frac{P}{T}v\right) - \frac{1-\varepsilon}{\varepsilon}\frac{RT}{P}\sum_{i=1}^{n_{comp}}\frac{\partial q_i}{\partial t} \tag{A.3}$$

The rate of adsorption is described by the LDF model as

$$\frac{\partial q_i}{\partial t} = k_i(q_i^* - q_i) \tag{A.4}$$

where q_i^* is the solid phase equilibrium concentration which is calculated from the equilibrium isotherm model. The isotherm can be generalized as a function of fluid phase concentration and temperature:

$$q_i^* = f(c_i, T) \tag{A.5}$$

The pressure drop along the length of the column is calculated from Darcy's law:

$$-\frac{\partial P}{\partial z} = \frac{150}{4}\frac{1}{r_p^2}\left(\frac{1-\varepsilon}{\varepsilon}\right)^2 \mu v \tag{A.6}$$

Rearranging eq A.6 provides eq A.7 to evaluate the local velocity:

$$v = \frac{4}{150\mu}\left(\frac{\varepsilon}{1-\varepsilon}\right)^2 r_p^2\left(\frac{-\partial P}{\partial z}\right) \tag{A.7}$$

where r_p is the radius of the solid particles and μ is the fluid viscosity coefficient, which is assumed to be independent of temperature.

The one-dimensional energy balance equation, accounting for convection and dispersion along the axial direction in the packed bed, conduction along the column wall, and heat transfer between the bed and column wall, is given by

$$\left[\frac{1-\varepsilon}{\varepsilon}\left(\rho_s C_{p,s} + C_{p,a}\sum_{i=1}^{n_{comp}}q_i\right)\right]\frac{\partial T}{\partial t}$$
$$= \frac{K_z}{\varepsilon}\frac{\partial^2 T}{\partial z^2} - \frac{C_{p,g}}{R}\frac{\partial}{\partial z}(vP) - \frac{C_{p,g}}{R}\frac{\partial P}{\partial t}$$
$$- \frac{1-\varepsilon}{\varepsilon}C_{p,a}T\sum_{i=1}^{n_{comp}}\frac{\partial q_i}{\partial t} + \frac{1-\varepsilon}{\varepsilon}\sum_{i=1}^{n_{comp}}\left((-\Delta H_i)\frac{\partial q_i}{\partial t}\right)$$
$$- \frac{2h_{in}}{\varepsilon r_{in}}(T - T_w) \tag{A.8}$$

where $C_{p,g}$, $C_{p,s}$, and $C_{p,a}$ are the heat capacities of the fluid phase, solid phase, and the adsorbed phase, respectively; T_w is the wall temperature; r_{in} is the inner radius of the column; ρ_s and ρ_g are the densities of the particles and gas phase, respectively; ΔH_i is heat of adsorption of component i; h_{in} is the overall heat transfer coefficient from column to wall; and K_z is the thermal conductivity of the bed in the axial direction.

Finally, the wall energy balance is expressed as

$$\rho_w C_{p,w} \frac{\partial T_w}{\partial t} = K_w \frac{\partial^2 T_w}{\partial z^2} + \frac{2r_{in}h_{in}}{r_{out}^2 - r_{in}^2}(T - T_w)$$
$$- \frac{2r_{out}h_{out}}{r_{out}^2 - r_{in}^2}(T_w - T_a) \qquad \text{(A.9)}$$

where ρ_w and $C_{p,w}$ are the density and heat capacity of the column wall, typically made of stainless steel. r_{out} is the column outer radius, and h_{out} is the film heat transfer coefficient between the column wall and the ambient air.

A.2. Initial and Boundary Conditions

In order to describe the initial and boundary conditions, it is useful to consider the different steps that constitute a typical PSA cycle that are shown in Figure 2. For a cyclic adsorption process a convenient initial condition for the first step is either a bed equilibrated with the lighter component or the feed mixture at the feed temperature at a specified pressure. Thereafter, the finial conditions of one step constitute the initial conditions for the subsequent step.

In order to generalize the boundary conditions, it is convenient to describe the steps shown in Figure 2 by the position of the solenoid valves at the two ends of the adsorber in the direction of flow as open−closed, open−open, and closed−open, respectively.

Open−Open: The open−open case represents the operation in which there is gas flow through the column, such as the high pressure adsorption step. In this step, the pressure at the column exit is controlled by a back-pressure regulator and the inlet flow rate of the gas of known composition is controlled. For the component mass balance, Danckwert's boundary conditions for a dispersed plug flow system apply for the open−open case in Figure 2, where flow is from $z = 0$ to $z = L$:

$$D_L \left. \frac{\partial y_i}{\partial z} \right|_{z=0} = -v|_{z=0}(y_{i,\text{feed}} - y_i|_{z=0}) \qquad \text{(A.10)}$$

$$\left. \frac{\partial y_i}{\partial z} \right|_{z=L} = 0 \qquad \text{(A.11)}$$

The following boundary conditions for the energy balance equation are obtained by the analogy of mass and heat transfer:

$$K_z \left. \frac{\partial T}{\partial z} \right|_{z=0} = -\varepsilon v|_{z=0}\rho_g C_{p,g}(T_{\text{feed}} - T|_{z=0}) \qquad \text{(A.12)}$$

$$\left. \frac{\partial T}{\partial z} \right|_{z=L} = 0 \qquad \text{(A.13)}$$

The boundary conditions for the wall temperature are written assuming that the flanges at $z = 0$ and $z = L$ have a high thermal capacity so that their temperatures are well equilibrated with the ambient temperature, T_a. Hence

$$T_w|_{z=0} = T_a \qquad \text{(A.14)}$$

$$T_w|_{z=L} = T_a \qquad \text{(A.15)}$$

Since velocity is a function of the pressure gradient (through Darcy's law), the total mass balance equation is in effect second order in pressure; hence two boundary conditions are required. In a typical open−open operation, the pressure at the column exit is controlled using a regulator. Hence, the pressure at the exit of the column is set at the operating pressure, P_H:

$$P|_{z=L} = P_H \qquad \text{(A.16)}$$

Further, in a typical operation, the flow rate at the column inlet is controlled and hence the velocity is assigned a fixed value, v_{feed}:

$$v|_{z=0} = v_{\text{feed}} \qquad \text{(A.17)}$$

The inlet pressure is calculated from Darcy's law using the inlet velocity, which is controlled in this step.

Open−Closed: The open−closed case in Figure 2 is representative of a pressurization step. For the open−closed case in Figure 2, the boundary conditions for y and T are identical to those for the open−open case; i.e., eqs A.10−A.15 are applicable. The velocity at $z = 0$, $v|_{z=0}$, is calculated based on the change in pressure at the column inlet. The velocity at the closed end is zero. Hence, the pressure boundary condition at $z = L$ can be described by the following:

$$\left. \frac{\partial P}{\partial z} \right|_{z=L} = 0 \qquad \text{(A.18)}$$

Closed−Open: In the closed−open case, the end at $z = 0$ is closed and that at $z = L$ is open and gas flows out through $z = L$. Such situations are encountered during the forward blowdown step where the column is depressurized through $z = L$ to a lower pressure, either above atmospheric or subatmospheric using a vacuum pump. The boundary conditions eqs A.11 and A.13−A.15 are not affected, while eqs A.10 and A.12 are reduced to

$$\left. \frac{\partial y_i}{\partial z} \right|_{z=0} = 0 \qquad \text{(A.19)}$$

$$\left. \frac{\partial T}{\partial z} \right|_{z=0} = 0 \qquad \text{(A.20)}$$

Since $v|_{z=0} = 0$, the boundary condition for pressure is

$$\left. \frac{\partial P}{\partial z} \right|_{z=0} = 0 \qquad \text{(A.21)}$$

$v|_{z=L}$ is calculated from the change in pressure at the column outlet. A PVSA/VSA cycle has steps which are executed in the reverse direction; i.e., the flow is from $z = L$ to $z = 0$. For such steps, the boundary conditions discussed above for forward flow will apply with their ends interchanged.

■ ASSOCIATED CONTENT

ⓢ Supporting Information

Dimensionless coefficients in the governing equations and summary of boundary conditions for pressurization, adsorption, blowdown, and evacuation steps in the four-step PSA cycle. This material is available free of charge via the Internet at http://pubs.acs.org.

■ AUTHOR INFORMATION

Corresponding Author

*Tel.: +65 6316 8813 (A.R.); +65 6516 6545 (S.F.). Fax: +65 6794 7553 (A.R.); +65 6779 1936 (S.F.). E-mail: arvind@ntu.edu.sg (A.R.); chesf@nus.edu.sg (S.F.).

Notes

The authors declare no competing financial interest.

■ ACKNOWLEDGMENTS

■ NOMENCLATURE

A = cross-sectional area of the column $[\text{m}^2]$

b_0 = parameter in Langmuir isotherm $[\text{m}^3\ \text{mol}^{-1}]$

c = fluid phase concentration $[\text{mol}\ \text{m}^{-3}]$

$C_{p,a}$ = specific heat capacity of the adsorbed phase $[\text{J}\ \text{mol}^{-1}\ \text{K}^{-1}]$

$C_{p,g}$ = specific heat capacity of the gas phase $[\text{J}\ \text{mol}^{-1}\ \text{K}^{-1}]$

$C_{p,s}$ = specific heat capacity of the adsorbent $[\text{J}\ \text{kg}^{-1}\ \text{K}^{-1}]$

$C_{p,w}$ = specific heat capacity of the column wall $[\text{J}\ \text{kg}^{-1}\ \text{K}^{-1}]$

d_0 = parameter in Langmuir isotherm $[\text{m}^3\ \text{mol}^{-1}]$

D_L = axial dispersion $[\text{m}^2\ \text{s}^{-1}]$

D_m = molecular diffusivity $[\text{m}^2\ \text{s}^{-1}]$

D_p = macropore diffusivity $[\text{m}^2\ \text{s}^{-1}]$

E = energy consumption of vacuum pump or compressor $[\text{J}]$

f = state variable

f_j = cell average of state variable f

h_{in} = inside heat transfer coefficient $[\text{J}\ \text{m}^{-2}\ \text{K}^{-1}\ \text{s}^{-1}]$

h_{out} = outside heat transfer coefficient $[\text{J}\ \text{m}^{-2}\ \text{K}^{-1}\ \text{s}^{-1}]$

H = enthalpy $[\text{J}\ \text{mol}^{-1}]$

J = error $[\%]$

k = mass transfer coefficient $[\text{s}^{-1}]$

K_w = thermal conductivity of column wall $[\text{J}\ \text{m}^{-1}\ \text{K}^{-1}\ \text{s}^{-1}]$

K_z = effective gas thermal conductivity $[\text{J}\ \text{m}^{-1}\ \text{K}^{-1}\ \text{s}^{-1}]$

L = column length $[\text{m}]$

mole = number of moles $[\text{mol}]$

n_{comp} = number of components

n_{cycle} = number of VSA cycle

n_{DV} = number of decision variables

N = number of discretization volumes

P = pressure $[\text{Pa}]$

Pe = Peclet number

Pe_h = heat Peclet number

$\overline{P}$ = dimensionless pressure

q = concentration in the solid phase $[\text{mmol}\ \text{g}^{-1}]$

q_{sb} = saturation concentration in the solid phase for site 1 $[\text{mmol}\ \text{g}^{-1}]$

q_{sd} = saturation concentration in the solid phase for site 2 $[\text{mmol}\ \text{g}^{-1}]$

r_{in} = column inner radius $[\text{m}]$

r_{out} = column outer radius $[\text{m}]$

r_p = particle radius $[\text{m}]$

R = universal gas constant $[\text{Pa}\ \text{m}^3\ \text{mol}^{-1}\ \text{K}^{-1}]$

t = time $[\text{s}]$

T = temperature $[\text{K}]$

T_a = ambient temperature $[\text{K}]$

T_w = column wall temperature $[\text{K}]$

$\overline{T}$ = dimensionless temperature

U = internal energy $[\text{J}\ \text{mol}^{-1}]$

v = interstitial velocity $[\text{m}\ \text{s}^{-1}]$

V = cell volume $[\text{m}^3]$

$\overline{v}$ = dimensionless interstitial velocity

x = dimensionless solid phase concentration

x^* = dimensionless equilibrium concentration in solid phase

y = composition in the gas phase

z = bed coordinate $[\text{m}]$

Z = dimensionless axial coordinate

Greek Symbols

ε = bed voidage

ε_p = particle voidage

η = compression/evacuation effciency

γ = adiabatic constant

λ = rate of pressure change $[\text{s}^{-1}]$

μ = fluid viscosity $[\text{kg}\ \text{m}^{-1}\ \text{s}^{-1}]$

ρ_g = density of fluid phase $[\text{mol}\ \text{m}^{-3}]$

ρ_s = density of adsorbent $[\text{kg}\ \text{m}^{-3}]$

ρ_w = wall density $[\text{kg}\ \text{m}^{-3}]$

Π = dimensionless group in column wall energy balance

τ = dimensionless time

τ' = tortuosity

Ω = dimensionless group in column energy balance

ψ = dimensionless group in component and total mass balance equations

σ = dimensionless group in column energy balance

Subscripts

0 = reference value for nondimensionalizing parameters

acc = accumulation

ads = adsorption step

bd = blowdown step

evac = evacuation step

EB = energy balance

f = flue gas

feed = feed condition

gen = generated

H = high

i = index of component

in = stream coming in

I = intermediate

j = index of cell volume

L = low

MB = mass balance

out = stream coming out

press = pressurization step

ref = reference

T = total

■ REFERENCES

(1) MIT. *The Future of Coal*; 2007. http://web.mit.edu/coal/.

(2) Zhang, J.; Webley, P.; Xiao, P. Effect of process parameters on power requirements of vacuum swing adsorption technology for CO_2 capture from flue gas. *Energy Convers. Manage.* **2008**, *49*, 346−356.

(3) Zhang, J.; Webley, P. Cycle development and design for CO_2 capture from flue gas by vacuum swing adsorption. *Environ. Sci. Technol.* **2008**, *42*, 563−569.

(4) Ebner, A.; Ritter, J. State-of-the-art Adsorption and Membrane Separation Processes for Carbon Dioxide Production from Carbon Dioxide Emitting Industries. *Sep. Sci. Technol.* **2009**, *44*, 1273−1421.

(5) Ruthven, D. M. *Principles of Adsorption and Adsorption Processes*; Wiley Interscience: New York, 1984.

(6) Farooq, S.; Ruthven, D. Numerical simulation of a kinetically controlled pressure swing adsorption bulk separation process based on a diffusion model. *Chem. Eng. Sci.* **1991**, *46*, 2213−2224.

(7) Sircar, S.; Rao, M.; Golden, T. In *Studies in Surface Science and Catalysis*; Dbrowski, A., Ed.; Elsevier: Amsterdam, 1999; Vol. *120*, Part A; pp 395−423.

(8) Lemcoff, N. In *Studies in Surface Science and Catalysis*; van Santen, R., van Leeuwen, P. W. N. M., Moulijn, J. A., Averill, B. A., Eds.; Elsevier: Amsterdam, 1999; Vol. *123*; pp 459−485.

(9) Raghavan, N.; Hassan, M.; Ruthven, D. Numerical simulation of a PSA system using a pore diffusion model. *Chem. Eng. Sci.* **1986**, *41*, 2787−2793.

(10) Ritter, J.; Yang, R. Pressure swing adsorption: experimental and theoretical study on air purification and vapor recovery. *Ind. Eng. Chem. Res.* **1991**, *30*, 1023−1032.

(11) Malek, A.; Farooq, S. Hydrogen purification from refinery fuel gas by pressure swing adsorption. *AIChE J.* **1998**, *44*, 1985−1992.

(12) Sircar, S.; Golden, T. Purification of Hydrogen by Pressure Swing Adsorption. *Sep. Sci. Technol.* **2000**, *35*, 667−687.

(13) Grande, C.; Rodrigues, A. Propane/Propylene Separation by Pressure Swing Adsorption Using Zeolite 4A. *Ind. Eng. Chem. Res.* **2005**, *44*, 8815−8829.

(14) Kapoor, A.; Yang, R. Kinetic separation of methanecarbon dioxide mixture by adsorption on molecular sieve carbon. *Chem. Eng. Sci.* **1989**, *44*, 1723−1733.

(15) Sircar, S. Pressure Swing Adsorption. *Ind. Eng. Chem. Res.* **2002**, *41*, 1389−1392.

(16) Na, B.-K.; Lee, H.; Koo, K.-K.; Song, H. Effect of Rinse and Recycle Methods on the Pressure Swing Adsorption Process To Recover CO_2 from Power Plant Flue Gas Using Activated Carbon. *Ind. Eng. Chem. Res.* **2002**, *41*, 5498−5503.

(17) Kikkinides, E.; Yang, R.; Cho, S. Concentration and recovery of carbon dioxide from flue gas by pressure swing adsorption. *Ind. Eng. Chem. Res.* **1993**, *32*, 2714−2720.

(18) Chaffee, A.; Knowles, G.; Liang, Z.; Zhang, J.; Xiao, P.; Webley, P. CO_2 capture by adsorption: Materials and process development. *Int. J. Greenhouse Gas Control* **2007**, *1*, 11−18.

(19) Ko, D.; Siriwardane, R.; Biegler, L. Optimization of pressure swing adsorption and fractionated vacuum pressure swing adsorption processes for CO_2 capture. *Ind. Eng. Chem. Res.* **2005**, *44*, 8084−8094.

(20) Agarwal, A.; Biegler, L.; Zitney, S. Superstructure-Based Optimal Synthesis of Pressure Swing Adsorption Cycles for Precombustion CO_2 Capture. *Ind. Eng. Chem. Res.* **2009**, *49*, 5066−5079.

(21) Agarwal, A.; Biegler, L. T.; Zitney, S. E. A superstructure-based optimal synthesis of PSA cycles for post-combustion CO_2 capture. *AIChE J.* **2010**, *56*, 1813−1828.

(22) Carter, J. W.; Wyszynski, M. L. The pressure swing adsorption drying of compressed air. *Chem. Eng. Sci.* **1983**, *38*, 1093−1099.

(23) Raghavan, N. S.; Ruthven, D. M. Numerical simulation of a fixed-bed adsorption column by the method of orthogonal collocation. *AIChE J.* **1983**, *29*, 922−925.

(24) Kikkinides, E.; Yang, R. Effects of bed pressure drop on isothermal and adiabatic adsorber dynamics. *Chem. Eng. Sci.* **1993**, *48*, 1545−1555.

(25) Kaczmarski, K.; Mazzotti, M.; Storti, G.; Morbidelli, M. Modeling fixed-bed adsorption columns through orthogonal collocations on moving finite elements. *Comput. Chem. Eng.* **1997**, *21*, 641−660.

(26) Webley, P.; He, J. Fast solution-adaptive finite volume method for PSA/VSA cycle simulation; 1 single step simulation. *Comput. Chem. Eng.* **2000**, *23*, 1701−1712.

(27) Todd, R.; He, J.; Webley, P.; Beh, C.; Wilson, S.; Lloyd, M. Fast Finite-Volume Method for PSA/VSA Cycle Simulation-Experimental Validation. *Ind. Eng. Chem. Res.* **2001**, *40*, 3217−3224.

(28) Cruz, P.; Santos, J. C.; Magalhães, F. D.; Mendes, A. Simulation of separation processes using finite volume method. *Comput. Chem. Eng.* **2005**, *30*, 83−98.

(29) LeVeque, R. *Finite Volume Methods for Hyperbolic Problems*; Cambridge University Press: Cambridge, U.K., 2002.

(30) Javeed, S.; Qamar, S.; Seidel-Morgenstern, A.; Warnecke, G. Efficient and accurate numerical simulation of nonlinear chromatographic processes. *Comput. Chem. Eng.* **2011**, *35*, 2294−2305.

(31) Medi, B.; Amanullah, M. Application of a Finite-Volume Method in the Simulation of Chromatographic Systems: Effects of Flux Limiters. *Ind. Eng. Chem. Res.* **2010**, *50*, 1739−1748.

(32) Jiang, G.-S.; Shu, C.-W. Efficient Implementation of Weighted ENO Schemes. *J. Comput. Phys.* **1996**, *126*, 202−228.

(33) Liu, X.-D.; Osher, S.; Chan, T. Weighted Essentially Non-oscillatory Schemes. *J. Comput. Phys.* **1994**, *115*, 200−212.

(34) Cruz, P.; Alves, M.; Magalhes, F.; Mendes, A. Solution of hyperbolic PDEs using a stable adaptive multiresolution method. *Chem. Eng. Sci.* **2003**, *58*, 1777−1792.

(35) Hassanzadeh, H.; Abedi, J.; Pooladidarvish, M. A comparative study of flux-limiting methods for numerical simulation of gas-solid reactions with Arrhenius type reaction kinetics. *Comput. Chem. Eng.* **2009**, *33*, 133−143.

(36) Farthing, M.; Miller, C. A comparison of high-resolution, finite-volume, adaptive-stencil schemes for simulating advective-dispersive transport. *Adv. Water Resour.* **2000**, *24*, 29−48.

(37) Sweby, P. K. High Resolution Schemes Using Flux Limiters for Hyperbolic Conservation Laws. *SIAM J. Numer. Anal.* **1984**, *21*, 995−1011.

(38) Krishnamurthy, S.; Haghpanah, R.; Rajendran, A.; Farooq, S. Adsorption and Diffusion of CO_2 and Nitrogen on 13X and Silica Gel. Presented at the 14th Asia Pacific Confederation of Chemical Engineering Congress [APCChE 2012], Singapore, Feb 21−24, 2012.

(39) *Quality Guidelines for Energy System Studies: CO_2 Impurity Design Parameters*; National Energy Technology Laboratory Report, DOE/NETL-341/011212; 2012.